

¹ European Electricity Grids May Exhibit
² Heatwave-induced Capacity Bottlenecks

³ Enming Liang¹, Minghua Chen^{1,2*}, Srinivasan Keshav^{3*}

⁴ ¹Department of Data Science, City University of Hong Kong.

⁵ ²School of Data Science, The Chinese University of Hong Kong
(Shenzhen).

⁶ ³Department of Computer Science and Technology, University of
⁷ Cambridge.
⁸

⁹ *Corresponding author(s). E-mail(s): minghua.chen@cityu.edu.hk;
¹⁰ sk818@cam.ac.uk;

¹¹ Contributing authors: eliang4-c@my.cityu.edu.hk;

¹² **Supplementary Information**

¹³ This Supplementary Information provides detailed methodological settings, extended
¹⁴ results, and comprehensive validation studies that substantiate the main findings
¹⁵ presented in the manuscript.

16 Contents

17	1 Detailed Data Source	3
18	2 Detailed Problem Formulations	3
19	2.1 Alternating Current (AC)-OPF	3
20	2.2 Security-Constrained (SC)-OPF	4
21	2.3 Temperature-Dependent (TD)-OPF	5
22	3 EU Simulation Settings	6
23	3.1 Setting Overview	6
24	3.2 Demand Calibration	8
25	3.3 Generator Derating Effects	10
26	3.4 Conductor Thermal Models	10
27	3.4.1 Single Conductor Heat Balance	10
28	3.4.2 Conductor Thermal Limits	11
29	3.4.3 Multi-Bundle Heat Balance	12
30	3.5 Heatwave Generation	14
31	4 EU Simulation Results	20
32	4.1 Setup	20
33	4.2 Heat-flow Analysis for Single Country	20
34	4.2.1 Spain	23
35	4.2.2 Italy	26
36	4.2.3 France	29
37	4.3 Cross-Border Analysis for Multiple Countries	32
38	4.3.1 Spain and Neighboring Countries	33
39	4.3.2 France and Neighboring Countries	35
40	5 IEEE Benchmark Simulation	37

41 1 Detailed Data Source

42 Table 1 summarises the publicly available datasets used in this study, encompassing
 43 the European transmission network topology, historical and projected weather data,
 44 electricity demand profiles, and renewable generation models.

Supplementary Table 1 | Summary of data sources.

Data	Description
PGLIB	IEEE Testing Grid files
PyPSA-Eur [1]	Open-source dataset and configurations of European transmission network
ERA5 [2]	1940 to present hourly global climate data from ECMWF reanalysis
C3S [3]	2005 to 2100 reference climate data from C3S Energy operational service
ENTSO-E [4]	Historical hourly country-level power demand data
Demand.ninja [5]	Weather-dependent energy demand models
Atlite [6]	Open-source model for renewable generation calculation

45 2 Detailed Problem Formulations

46 This section presents three optimal power flow (OPF) formulations featured in
 47 the main text: the baseline alternating current (AC)-OPF, the security-constrained
 48 (SC)-OPF, and our temperature-dependent (TD)-OPF model. We also describe the
 49 simplified variants and combinations employed in the case studies.

50 2.1 Alternating Current (AC)-OPF

51 We adopt the standard AC-OPF formulation [7] as the baseline in our case studies:

$$\min \sum_{i \in \mathcal{N}} \sum_{k \in \mathcal{G}_i} c_{i,k} \cdot P_{i,k}, \quad (1)$$

s.t.

$$\text{Power flow balance} \quad \begin{cases} \sum_{k \in \mathcal{G}_i} P_{i,k} - P_i^d = \operatorname{re} \left(V_i \left(\sum_{j \in \mathcal{N}} Y_{ij} V_j \right)^* \right) \\ \sum_{k \in \mathcal{G}_i} Q_{i,k} - Q_i^d = \operatorname{im} \left(V_i \left(\sum_{j \in \mathcal{N}} Y_{ij} V_j \right)^* \right) \end{cases}, \quad \forall i \in \mathcal{N}, \quad (2)$$

$$\text{Line flow limits} \quad |V_i ((V_i - V_j) Y_{ij})^*| \leq S_{ij}^{\max}, \quad \forall (i, j) \in \mathcal{L}, \quad (3)$$

$$\text{Generation limits} \quad P_{i,k} \in [P_{i,k}^{\min}, P_{i,k}^{\max}], Q_{i,k} \in [Q_{i,k}^{\min}, Q_{i,k}^{\max}], \quad \forall i \in \mathcal{N}, \forall k \in \mathcal{G}_i, \quad (4)$$

$$\text{Voltage limits} \quad |V_i| \in [V_m^{\min}, V_m^{\max}], |\angle V_{ij}| \leq V_a^{\max}, \quad \forall i \in \mathcal{N}, \forall (i, j) \in \mathcal{L}, \quad (5)$$

var. \mathbf{P} , \mathbf{Q} , and \mathbf{V} .

52 Detailed parameter descriptions are provided in Table 2.

53 In contrast to the linearized DC-OPF models commonly adopted in power system
 54 tools (e.g., PyPSA [1]), AC-OPF explicitly captures transmission line thermal losses
 55 and resistance variations—both essential for accurate conductor thermal modeling in
 56 temperature-dependent analysis.

Supplementary Table 2 | Parameters of the power grid model.

Notation	Description
\mathcal{T}	set of time slots
\mathcal{N}	set of buses
\mathcal{L}	set of lines
\mathcal{C}	set of contingency of line outage
$\mathcal{G}_i, \forall i \in \mathcal{N}$	set of generators at each bus
$\mathcal{S}_l, \forall l \in \mathcal{L}$	set of segments at each line
$V_i, \forall i \in \mathcal{N}$	complex voltage at each bus
$P_i^d, Q_i^d, \forall i \in \mathcal{N}$	active and reactive power demand at each bus
$P_{i,k}, Q_{i,k}, \forall i \in \mathcal{N}, \forall k \in \mathcal{N}_i$	active and reactive power generation for each generator
$c_{i,k}, \forall i \in \mathcal{N}, \forall k \in \mathcal{N}_i$	generation cost for each generator
$P_l, Q_l, I_l, \forall l = (i, j) \in \mathcal{L}$	active, reactive power flow and current at each line
$T_{l,s}, \forall l \in \mathcal{L}, \forall s \in \mathcal{S}_l$	temperature for each segment at each line
$d_{l,s}, \forall l \in \mathcal{L}, \forall s \in \mathcal{S}_l$	length for each segment at each line
$Y_l, G_l, B_l, R_l, X_l, \forall l \in \mathcal{L}$	admittance, conductance, susceptance, resistance, reactance

57 AC-OPF is typically employed in single-snapshot formulations [8], as the non-linear
 58 constraints render multi-period extensions computationally prohibitive. Linearized
 59 DC-OPF models, by contrast, are better suited for multi-period formulations in long-
 60 term planning applications, where temporal trade-offs take precedence over detailed
 61 power flow accuracy [9].

62 2.2 Security-Constrained (SC)-OPF

63 Security constraints are critical operational requirements for power systems. The N -1
 64 security criterion, which ensures that the system remains within safe operating limits
 65 following any single transmission line outage, is widely adopted in practice [10]. Let \mathcal{C}
 66 denote the set of credible line outages that do not induce network disconnection. The
 67 standard SC-OPF is formulated as:

$$\begin{aligned} & \min \quad (1) \\ & \text{s.t.} \end{aligned} \tag{6}$$

Base-case constraints (2) – (5),

$$\text{Cont. PF balance} \quad \begin{cases} \sum_{k \in \mathcal{G}_i} P_{i,k}^c - P_i^d = \operatorname{re} \left(V_i (\sum_{j \in \mathcal{N}} Y_{ij}^c V_j^c)^* \right) \\ \sum_{k \in \mathcal{G}_i} Q_{i,k}^c - Q_i^d = \operatorname{im} \left(V_i (\sum_{j \in \mathcal{N}} Y_{ij}^c V_j^c)^* \right) \end{cases}, \forall i \in \mathcal{N}, c \in \mathcal{C} \tag{7}$$

$$\text{Cont. line flow limits} \quad |V_i^c ((V_i^c - V_j^c) Y_{ij}^c)^*| \leq S_{ij}^{\max}, \forall (i, j) \in \mathcal{L}, c \in \mathcal{C} \tag{8}$$

$$\text{Cont. generation limits} \quad P_{i,k}^c \in [P_{i,k}^{\min}, P_{i,k}^{\max}], Q_{i,k}^c \in [Q_{i,k}^{\min}, Q_{i,k}^{\max}], \forall i \in \mathcal{N}, \forall k \in \mathcal{G}_i, c \in \mathcal{C} \tag{9}$$

$$\text{Cont. voltage limits} \quad |V_i^c| \in [V_m^{\min}, V_m^{\max}], |\angle V_{ij}^c| \leq V_a^{\max}, \forall i \in \mathcal{N}, \forall (i, j) \in \mathcal{L}, c \in \mathcal{C} \tag{10}$$

$$\text{Ramping limits} \quad \|\mathbf{P} - \mathbf{P}^c\|_\infty \leq \Delta_p, \|\mathbf{Q} - \mathbf{Q}^c\|_\infty \leq \Delta_q, \|\mathbf{V} - \mathbf{V}^c\|_\infty \leq \Delta_v, \forall c \in \mathcal{C} \tag{11}$$

Base-case var. \mathbf{P}, \mathbf{Q} , and \mathbf{V} , Cont. var. $\mathbf{P}^c, \mathbf{Q}^c$, and $\mathbf{V}^c, \forall c \in \mathcal{C}$

68 Detailed parameter descriptions are provided in Table 2.

69 The security constraints (7)–(11) enforce feasibility under all post-contingency
 70 states. Base-case and post-contingency variables are coupled through ramping con-
 71 straints: under preventive control settings, real power generation (over non-slack buses)
 72 is fixed ($\Delta_p = 0$), whereas under corrective control settings, all decision variables may
 73 adjust within prescribed bounds.

74 Since the number of variables and constraints scales linearly with the number
 75 of contingencies, existing approaches focus on simplifying the security formulation.
 76 Common strategies include applying a fixed percentage reduction (e.g., 70%) to branch
 77 flow limits in basic AC-OPF to provide implicit security margins [11], or employing the
 78 Line-Outage-Distribution-Factor (LODF) to calculate a contingency-informed security
 79 margin on the branch flow limits [12].

80 In the IEEE 30-bus experiments, we implement the complete AC-based N -1 pre-
 81 ventive security constraints, as the exact network topology is available and the problem
 82 remains computationally tractable. For the large-scale European grid analysis, we
 83 adopt the commonly used 70% fixed security margin [1] due to (i) inexact topology
 84 resulting from network clustering and (ii) computational limitations.

85 2.3 Temperature-Dependent (TD)-OPF

86 Standard AC-OPF neither incorporates the influence of weather conditions on electri-
 87 cal network parameters, such as conductor resistance, nor accounts for the dynamic
 88 thermal limits of transmission lines. Temperature-dependent OPF (TD-OPF) for-
 89 mulations [13–15] address these limitations by integrating transmission line thermal
 90 modeling:

$$\begin{aligned} \min & \quad (1) \\ \text{s.t.} & \\ \text{AC-OPF constraints} & \quad (2) - (5), \\ \text{Heat balance equations} & \quad T_{l,s} = \mathcal{H}(I_l, \mathcal{W}_{l,s}), \forall s \in \mathcal{S}_l \quad (12) \\ \text{Conductor thermal limits} & \quad T_{l,s} \leq T^{\max}, \forall s \in \mathcal{S}_l \quad (13) \\ \text{Line resistance} & \quad R_l = \sum_{s \in \mathcal{S}_l} d_{l,s} \cdot R(T_{l,s}) \quad (14) \\ \text{Line current flow} & \quad I_l = |(V_i - V_j)Y_{ij}|, \forall l = (i, j) \in \mathcal{L}, \quad (15) \\ \text{Line admittance} & \quad Y_l = 1/(R_l + i \cdot X_l), \forall l = (i, j) \in \mathcal{L}, \quad (16) \\ \text{var.} & \quad \mathbf{P}, \mathbf{Q}, \text{ and } \mathbf{V}. \end{aligned}$$

91 Detailed parameter descriptions are provided in Table 2.

92 Beyond the standard AC-OPF constraints, the TD-OPF formulation captures
 93 conductor thermal behaviour and enforces thermal limits under specific weather con-
 94 ditions. The model computes steady-state line temperatures through non-linear heat
 95 balance equations, subject to maximum allowable temperature constraints (e.g., 90°C).
 96 Line temperature directly determines conductor resistance, thereby altering network
 97 admittance and influencing power flow solutions. This bidirectional coupling between
 98 power flow and heat flow via line current renders the exact TD-OPF computationally
 99 demanding.

100 Existing studies have proposed various simplifications to reduce computational
 101 complexity. In dynamic line rating (DLR) applications [16–19], thermal limits are
 102 considered and transformed into current flow constraints:

$$I_l \leq I_{l,s}^{\max} = \mathcal{H}^{-1}(T^{\max}, W_{l,s}) \quad (17)$$

103 where T^{\max} is the maximum allowable conductor temperature, I_l is the current flow
 104 magnitude on line l , $I_{l,s}^{\max}$ is the maximum allowable current flow over line seg-
 105 ment (l, s) , $W_{l,s}$ represents the weather conditions over the line segment, and \mathcal{H}^{-1}
 106 is the inverse heat balance equation that determines the maximum current given the
 107 temperature limit and weather conditions.

108 The current constraints are then reformulated as branch power-flow constraints
 109 by multiplying them by the voltage magnitude. Such DLR formulations are typically
 110 employed in linearized OPF models without dynamic coupling between power flow
 111 and heat balance equations.

112 Alternatively, conductor thermal behavior can be approximated using a polynomial
 113 function based on Joule heating effects, such that thermal limits are expressed as [20]:

$$\beta_0(W_l) + \beta_1(W_l)I_l^2 + \beta_2(W_l)I_l^4 \leq T^{\max} \quad (18)$$

114 where the coefficients β_0 , β_1 , and β_2 are functions of the average weather conditions
 115 W_l along the transmission line, and I_l is the current flow magnitude on line l .

116 3 EU Simulation Settings

117 3.1 Setting Overview

118 To assess the resilience of the European electricity grid under projected future heat-
 119 wave conditions, we employ an integrated modeling approach that combines the data
 120 sources detailed in Table 1 (main text) with the computational framework described in
 121 Section 2 (main text). Our analysis focuses on Western European countries that have
 122 historically experienced substantial heatwave events, as detailed in Supplementary
 123 Table 3.

124 We then derive country-specific power grid representations using PyPSA-Eur work-
 125 flows [1, 11]. Country-specific power grid configurations and operational parameters
 126 are detailed in Supplementary Tables 4 and 5.

127 Our methodology begins by extracting the complete European grid topology and
 128 subsequently filtering for regions of interest. To address potential local modeling arte-
 129 facts—including misalignment of load and supply distributions and inadequate rep-
 130 resentation of urban underground transmission infrastructure—we adopt a clustered
 131 network approach supported by the PyPSA framework.

132 This clustering methodology consolidates proximate buses and transmission lines,
 133 thereby simplifying the grid representation while minimizing spurious transmission
 134 bottlenecks arising from modeling errors [1, 21]. The clustering procedure first dis-
 135 tributes the target number of clusters across countries in proportion to their electrical
 136 loads by solving an assignment problem that minimizes the deviation between integer

Supplementary Table 3 | Notable European Heatwave Records (in 2019 and 2022)

Country	Year	Temperature	Location
Spain	2019	44.4°C	Albuquerque, Badajoz
	2022	45.8°C	Torremocha del Campo
Portugal	2019	43.1°C	Alvega, Santarem
	2022	47.0°C	Pinhão
France	2019	46.0°C	Vérargues
	2022	42.6°C	Biscarrosse
Italy	2019	40.8°C	Rome
	2022	46.6°C	Perugia
Germany	2019	42.6°C	Lingen
	2022	40.3°C	Bad Mergentheim
UK	2019	38.7°C	Cambridge
	2022	40.3°C	RAF Coningsby
Belgium	2019	41.8°C	Begijnendijk
	2022	40.0°C	Kapelle-op-den-Bos
Netherlands	2019	40.7°C	Gilze-Rijen
	2022	39.5°C	Maastricht-Aachen Airport

¹ References: [2019 European heatwaves]; [2022 European heatwaves].

² Temperatures represent the highest recorded during each respective heatwave period

cluster assignments and the ideal proportional allocation. Weighted k-means clustering is then applied within each country separately, incorporating regional electrical load as weights to ensure that high-demand areas receive adequate representation in the simplified network topology [1, 21]. To balance computational efficiency with network fidelity, we adopt a 75% resolution clustered network relative to the initial 380 kV transmission network configuration. We apply the k-means clustering workflow in Pypsa-Eur to aggregate buses into larger geographical regions, preserving essential power flow patterns while reducing computational complexity [21].

This clustering addresses fundamental modeling artefacts present in ENTSO-E derived network topologies [1]. These topologies exhibit unrealistic load shedding even with sufficient generation capacity, stemming from two principal issues: (i) Voronoi cell assignments that inaccurately map loads and generators to substations, failing to represent actual distribution network topology; and (ii) underrepresentation of inner-city underground cabling. The 75% resolution effectively smooths these local assignment errors while preserving network characteristics critical for our analysis.

To incorporate weather-induced thermal limits, it is essential to model the physical properties and operational requirements of transmission lines. In our case study, we standardize transmission lines to the “Al/St 240/40 4-bundle 380.0” specification, featuring an aluminum/steel cross-section of 240/40 mm² and a 4-bundle configuration of wires per phase at 380 kV [1, 22]. Conventional aluminum/steel conductors (e.g., ACSR, AAC, AAAC) typically operate within temperature ranges of 80°C to 120°C [17, 23–25].

Supplementary Table 4 | Installed Capacity by Country and Technology Type

Country	Conv. ^a (GW)	Renew. ^b (GW)	Stor. ^c (GW)
Spain	39.99	67.89	23.79
Portugal	4.50	8.73	5.08
France	64.17	37.96	13.67
Italy	47.62	32.55	11.77
Germany	72.37	117.59	7.24
UK	49.91	51.54	0.66
Belgium	10.79	9.88	1.18
Netherlands	17.57	21.87	0.00

^a Conv. = Conventional (fossil fuel and nuclear power plants)

^b Renew. = Renewable (wind, solar, hydro, and biomass power plants)

^c Stor. = Storage units (battery and H2 storage units)

Note: Installed capacity remains constant across all resolution levels.

Supplementary Table 5 | Power Grid Configuration at Different Resolutions

Country	Buses	Lines	Number of Generator/Storage		
			Conv. ^a	Renew. ^b	Stor. ^c
Spain	281	442	91	339	75
Portugal	81	129	14	66	24
France	439	711	53	652	51
Italy	373	522	93	622	65
Germany	484	682	792	936	31
UK	319	426	90	451	6
Belgium	42	50	23	82	3
Netherlands	34	41	30	64	0

^a Conv. = Conventional (fossil fuel and nuclear power plants)

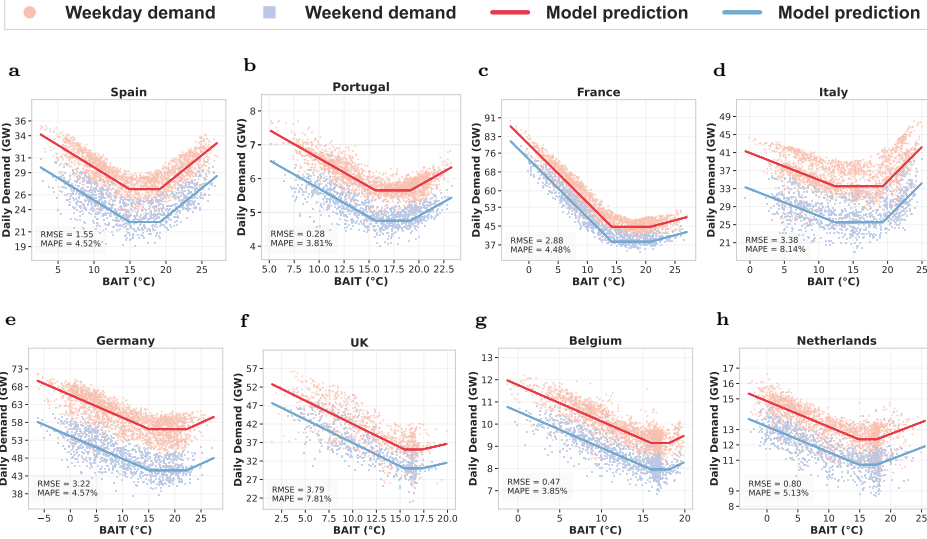
^b Renew. = Renewable (wind, solar, hydro, and biomass power plants)

^c Stor. = Storage units (battery and H2 storage units)

159 To address security constraints as operational requirements, we follow established
160 methodologies [16, 26] by implementing a simplified $N-1$ security criterion, limiting
161 transmission line flows to 70% of their maximum capacity. This approximation is jus-
162 tified by two considerations: first, the aggregated network topology does not perfectly
163 represent real-world grid configurations; second, full security-constrained optimization
164 with non-linear heat flow modeling becomes computationally intractable for large-scale
165 European network models.

166 3.2 Demand Calibration

167 We develop temperature-dependent electricity demand models following the
168 Demand.ninja framework [5], as detailed in Section 2.2 (main text). Since
169 Demand.ninja does not provide publicly available code for model calibration or raw
170 data processing, we implement their methodology [5] to calibrate demand models for
171 the European countries in our case study. We combine historical hourly load data from
172 ENTSO-E (2015–2024) with ERA5 reanalysis weather records, enabling us to capture
173 the complex, non-linear relationships between ambient temperature and electricity
174 consumption patterns across diverse European climatic zones.



Supplementary Figure 1 | Demand calibration for Western EU countries.

Supplementary Table 6 | Demand model calibration for Western European countries.

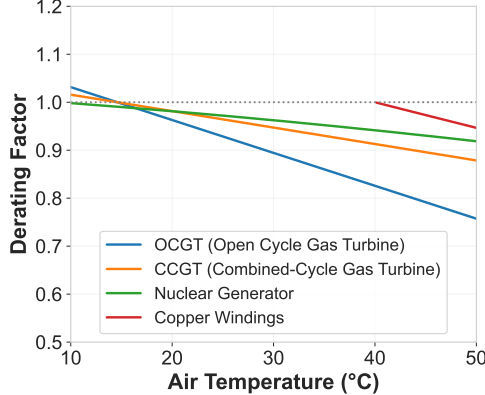
Country	P_{base} (GW)	P_{heat} (GW/°C)	P_{cool} (GW/°C)	T_{heat} (°C)	T_{cool} (°C)	α (GW)
Spain	22.32	0.60	0.79	14.93	19.16	4.45
Portugal	4.75	0.17	0.17	15.65	19.14	0.90
France	38.38	2.46	0.66	14.19	20.82	6.32
Italy	25.51	0.60	1.53	12.39	19.29	8.01
Germany	44.56	0.64	0.67	15.10	22.28	11.53
UK	30.02	1.26	0.58	15.46	17.32	5.10
Belgium	7.96	0.16	0.18	15.95	18.14	1.20
Netherlands	10.71	0.17	0.15	14.87	17.76	1.66

¹ Key parameters include baseline demand (P_{base}), heating coefficient (P_{heat}), cooling coefficient (P_{cool}), heating threshold temperature (T_{heat}), cooling threshold temperature (T_{cool}), and weekday demand difference coefficient (α).

² Demand models are calibrated based on historical hourly load data from 2015 to 2024 for all countries except Great Britain. Great Britain is calculated based on data from 2015 to 2020, given the availability of load data on the ENTSO-E platform.

175 We employ the open-source derivative-free optimizer PyPop7 [27] to calibrate the
 176 demand models and derive country-specific model parameters. Calibration results and
 177 model performance metrics are presented in Supplementary Figure 1 and Table 6.
 178 The results clearly identify cooling threshold temperatures and cooling load coeffi-
 179 cients under high-temperature conditions, providing a robust foundation for simulating
 180 temperature-induced demand changes under extreme heatwave scenarios.

181 For model calibration using historical data from 2015 to 2024, we exclude the
 182 growth rate parameter, yielding an average estimate of baseline country demand.



Supplementary Figure 2 | Generator derating factor under different temperatures. The capacity derating factor (η) for various generator types as a function of ambient temperature, showing how generating capacity diminishes during high-temperature events. This thermal sensitivity becomes particularly significant during heatwaves when multiple generators experience simultaneous capacity reductions.

For future scenario analysis, we incorporate variable annual growth rates (β) to represent different demand projection pathways. This approach accounts for emerging grid pressures from artificial intelligence infrastructure, smart home technologies, and electric vehicle adoption, all of which are expected to substantially alter historical demand patterns. By varying these growth rates, we evaluate grid performance under a range of electrification scenarios, spanning moderate to aggressive technology adoption trajectories.

3.3 Generator Derating Effects

As discussed in the main manuscript, generators experience derating with increasing temperatures during heatwaves, with the magnitude varying across different generator types and weather conditions. We quantify these thermal dependencies through a capacity derating factor $\eta \leq 1$ for conventional generators operating under elevated ambient temperatures ($T_{\text{amb}} \geq 20^{\circ}\text{C}$), as illustrated in Figure 2.

3.4 Conductor Thermal Models

3.4.1 Single Conductor Heat Balance

Heatwaves also reduce transmission capacity in power grids by affecting the thermal behavior of overhead conductors. This physical phenomenon can be modeled by the steady-state heat balance equation, which accounts for the equilibrium between heat generated by electrical current and solar radiation, and heat lost through convection, radiation, and conduction. The specific steady-state heat balance equation according

Supplementary Table 7 | Parameters in the conductor thermal model.

Notation	Description
ϕ	The angle between wind and axis of conductor, taking value in $[0, \pi/2]$
K_ϕ	Wind direction factor, $K_\phi = 1.194 - \cos(\phi) + 0.194 \cos(2\phi) + 0.368 \sin(2\phi)$
V_w	Wind speed [m/s]
D	Conductor diameter [m]
L	Conductor length [m]
S	Total solar heat intensity [W/m^2]
N_{re}	Dimensionless Reynolds number, $N_{\text{re}} = D\rho_f V_w / \mu_f$
ρ_f	Density of air [kg/m^3]
μ_f	Dynamic viscosity of air
λ_f	Thermal conductivity of air [$\text{W}/(\text{m} \cdot ^\circ\text{C})$]
α_{emi}	Radiation emissivity factor, taking values in $[0, 1]$
α_{abs}	Solar absorptivity factor, taking values in $[0, 1]$
α_r	Temperature-dependent resistance coefficient
σ_B	Stefan–Boltzmann constant $\sigma_B = 5.67 \times 10^{-8} [\text{W}/(\text{m}^2 \cdot \text{K}^4)]$
$T, T_{\text{amb}}, T_{\text{ref}}$	Conductor, ambient, and reference temperature [$^\circ\text{C}$]
$R(T_c)$	Unit temperature-dependent resistance [Ω/m]

203 to IEEE Std 738TM-2012 [28] used in our study is as follows:

$$\underbrace{H_C + H_R}_{\text{heat loss}} = \underbrace{H_S + H_J}_{\text{heat gain}} \quad [\text{W}/\text{m}], \quad (19)$$

204 where

$$H_C = \max \begin{cases} 3.645 \rho_f^{0.5} D^{0.75} (T - T_{\text{amb}})^{1.25}, & (\text{zero wind speed}); \\ K_\phi \left[1.01 + 1.35 N_{\text{re}}^{0.52} \right] \lambda_f (T - T_{\text{amb}}), & (\text{low wind speed}); \\ 0.754 K_\phi N_{\text{re}}^{0.6} \lambda_f (T - T_{\text{amb}}), & (\text{high wind speed}); \end{cases} \quad (20)$$

$$H_R = \pi \sigma_B D \alpha_{\text{emi}} \left[(T + 273)^4 - (T_{\text{amb}} + 273)^4 \right] \quad (21)$$

$$H_S = \alpha_{\text{abs}} D S \quad (22)$$

$$H_J = I^2 R(T) = I^2 R_{\text{ref}} (1 + \alpha_r (T - T_{\text{ref}})) \quad (23)$$

205 Here, H_C is the heat loss rate due to convective cooling affected by air temperature,
206 wind speeds, angles, and the conductor temperature; H_R is the heat loss rate due to
207 radiative cooling caused by the temperature difference, H_S is the heat gain rate due
208 to solar radiation and H_J is the heat gain rate due to Joule heating under conductor
209 current and temperature-dependent resistance. The values of these coefficients are
210 specified in Table 7.

211 3.4.2 Conductor Thermal Limits

212 Conductor thermal limits vary substantially across different technologies, as estab-
213 lished in the literature and industry standards (Table 8). Conventional conductors,
214 including Aluminum Conductor Steel Reinforced (ACSR), All Aluminum Conductor
215 (AAC), and All Aluminum Alloy Conductor (AAAC), typically operate within tem-
216 perature ranges of 80°C to 120°C [17, 23, 29]. In contrast, modern High Temperature
217 Low Sag (HTLS) conductors—such as Aluminum Conductor Steel Supported (ACSS),

Supplementary Table 8 | Summary of conductor thermal limits in literature.

Reference	Conductor Type	Thermal Limits
[23]	Conventional	80°C–120°C
[24]	ACSR	50°C–180°C
[29]	ACSR	90°C–110°C
[17]	Traditional (ACSR, AAC, AAAC) Modern (ACSS, ACCR, ZTACIR, ACCC)	<100°C 180°C–250°C
[25]	Conventional	80°C
[30]	HTLS	Up to 210°C
[1, 16]	Conventional	100°C

Aluminum Conductor Carbon Composite Reinforced (ACCR), ZTACIR, and Aluminum Conductor Carbon Core (ACCC)—are designed for continuous operation at significantly higher temperatures ranging from 180°C to 250°C [17].

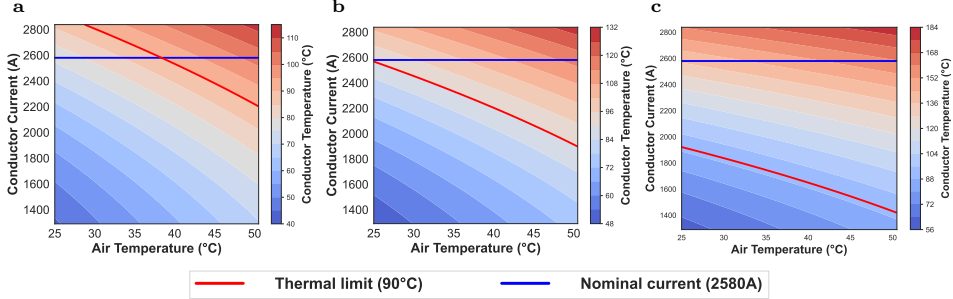
European transmission standards establish conservative operational limits for conventional conductors. According to ENTSO-E technical specifications [25], these conductors should not exceed 80°C under worst-case ambient conditions. Contemporary European network simulations, particularly PyPSA-based models of the EU transmission system [1, 16], typically adopt a 100°C maximum temperature limit for conventional conductors.

For this study, we set the maximum thermal limit for conventional conductors at 90°C, representing a balance between European standard limits and common simulation practices. This choice accounts for both operational safety margins and realistic network conditions.

High-temperature low-sag (HTLS) conductors, which permit substantially higher operating temperatures, remain limited primarily to pilot projects and small-scale field trials, such as those conducted in northern Germany and documented by ENTSO-E [30]. Thus, we focus our analysis on conventional conductor limits (90°C), given the currently limited deployment of HTLS conductors, and we conduct sensitivity analyses with varying thermal limits.

3.4.3 Multi-Bundle Heat Balance

In practice, multi-bundle transmission lines are commonly employed for long-distance power transmission, which significantly complicates thermal modeling due to mutual thermal interactions between conductors. The convective and radiative cooling of individual conductors is reduced when they are positioned in the wake of other conductors, creating complex heat transfer patterns that deviate from single-conductor assumptions. For instance, the PyPSA-Eur documentation specifies “Al/St 240/40 4-bundle 380.0” as the default conductor configuration for 380 kV transmission networks, representing a four-bundle conductor arrangement within a single transmission line. Such multi-bundle configurations are standard practice in high-voltage applications to reduce corona discharge and improve power transfer capacity.



Supplementary Figure 3 | Thermal analysis of Al/St 240/40 4-bundle 380 kV conductor under worst-case ambient conditions [25]. The conductor thermal equilibrium is evaluated at 0.6 m/s wind speed and 900 W/m² solar irradiance across varying ambient temperatures and current loads. Figures **a**, **b**, and **c** display steady-state conductor temperatures under individual, corrected, and merged conductor modeling frameworks, respectively.

Exact modeling of multi-conductor thermal behavior requires sophisticated finite-element simulations [31], which showed that steady-state temperatures of individual conductors within a bundle can vary by 5-25°C due to mutual thermal influences. This temperature variation has important implications for ampacity calculations and thermal limit assessments.

Given the computational complexity of exact modeling, two primary approaches are typically employed to simplify multi-conductor thermal analysis:

Individual Conductor Modeling (Fig. 3 (a)): One simplification approach neglects the mutual thermal influence among conductors and treats each bundle as an independent line [1], which is implemented in the dynamic line rating functionality of PyPSA. This simplification **overestimates** the transmission line capacity by failing to account for the reduced convective and radiative cooling effects that occur in multi-bundle configurations, where conductors shield each other from airflow and thermal radiation.

Merged Conductor Modeling (Fig. 3 (c)): An alternative simplification merges multiple bundles into a single equivalent transmission line, which neglects the physical spacing between individual conductors within the bundle. This single-line modeling approach is predominantly adopted in existing temperature-dependent optimal power flow (OPF) formulations [14, 32]. The method assumes uniform heat distribution and cooling across the entire conductor cross-section, which **underestimates** the transmission capacity due to convective cooling between the physical space of individual bundles.

Corrected Conductor Modeling (Fig. 3 (b)): To account for mutual thermal effects while maintaining computational efficiency in multi-bundle conductor modeling, we introduce a corrective factor applied to the cooling components H_C (convective cooling) and H_R (radiative cooling). Drawing from finite-element analysis results

274 reported in [31], which demonstrated that steady-state temperatures of individual con-
275 ductors within a bundle can vary by 5-25°C depending on their physical position due
276 to mutual thermal interactions, we adopt a correction factor of 0.8. The modified heat
277 balance equation becomes: $0.8 \cdot H_C + 0.8 \cdot H_R = H_S + H_J$. Under worst-case ambi-
278 ent conditions as defined by ENTSO-E [25]—0.6 m/s wind speed, 900 W/m² solar
279 irradiance, and maximum current flow—our model predicts that conductors reach the
280 90°C thermal limit at an ambient temperature of approximately 25°C. This corrected
281 capacity curve falls between the individual conductor and merged bundle modeling
282 approaches. Specifically, our results show approximately 15°C difference compared to
283 the individual conductor (optimistic setting) modeling approach, which aligns well
284 with the empirical finite-element analysis findings reported in [31].

285 We note that the physical conductor model serves as the reference for simulation
286 in the absence of real-world field test data. Nevertheless, we also compare corrected
287 conductor modeling with individual conductor modeling in the sensitivity analysis,
288 reflecting network performance under different physical model assumptions.

289 3.5 Heatwave Generation

290 We generate future European heatwave scenarios for 2026-2030 using the morphing
291 methodology detailed in Section 2.1 of the main manuscript. These projections build
292 upon historical extreme events—specifically the 2019, 2022, and 2024 heatwaves (e.g.,
293 Table 3)—which serve as baseline templates. Our approach combines hourly ERA5
294 reanalysis data (temperature, solar radiation, and wind speed) with future climate
295 projections from the Copernicus Climate Change Service (C3S) energy sector indica-
296 tors. This methodology preserves the spatial patterns and diurnal cycles of observed
297 extremes while incorporating climate change amplification factors. Temperature and
298 solar irradiance undergo additive bias correction in their original space, while wind
299 speed is morphed in log-space to ensure physically positive values.

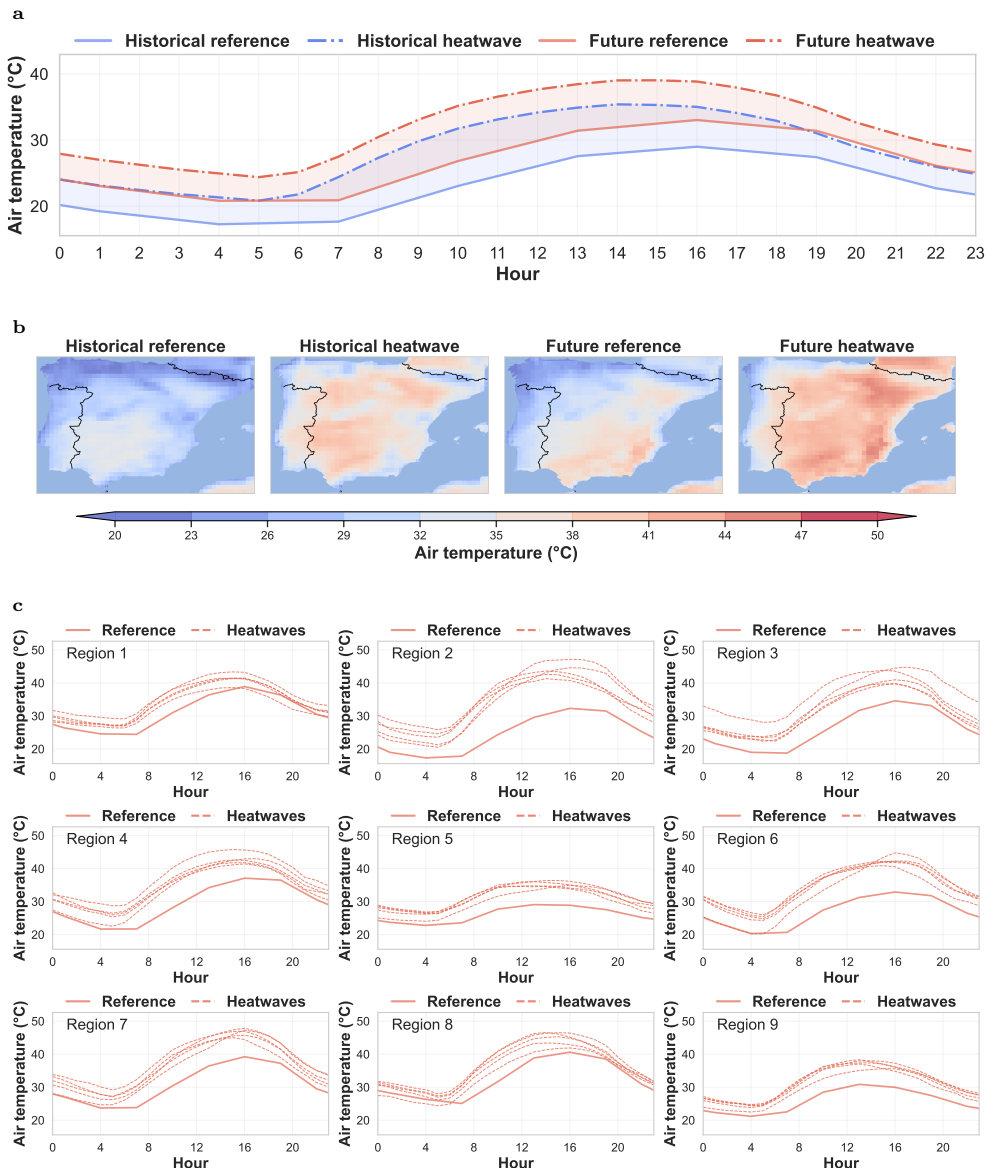
300 Generated weather variables for future heatwaves in Spain are presented in Figures
301 4 through 6. Each figure contains:

302 **a:** Demonstrates the morphing approach for simulating future heatwaves, where
303 delta values calculated from historical heatwave days (in July 2022) are applied to
304 future reference hot days.

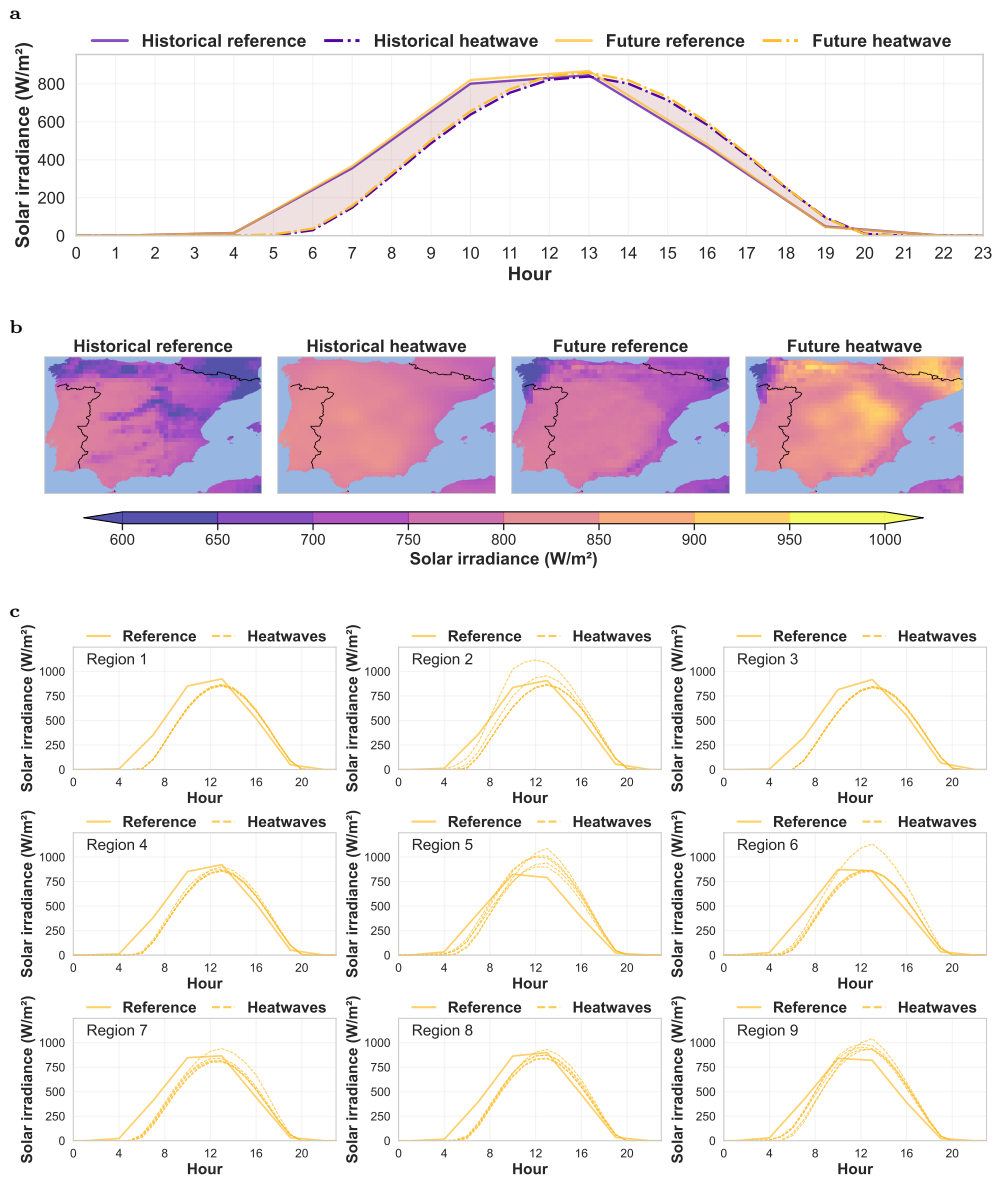
305 **b:** Shows spatial distributions of weather variables for both historical and future
306 reference conditions and their corresponding heatwaves.

307 **c:** Displays the 2030 heatwave scenarios generated using delta values from the five
308 hottest historical days, with separate visualizations for different sampled bus areas in
309 the electricity grid.

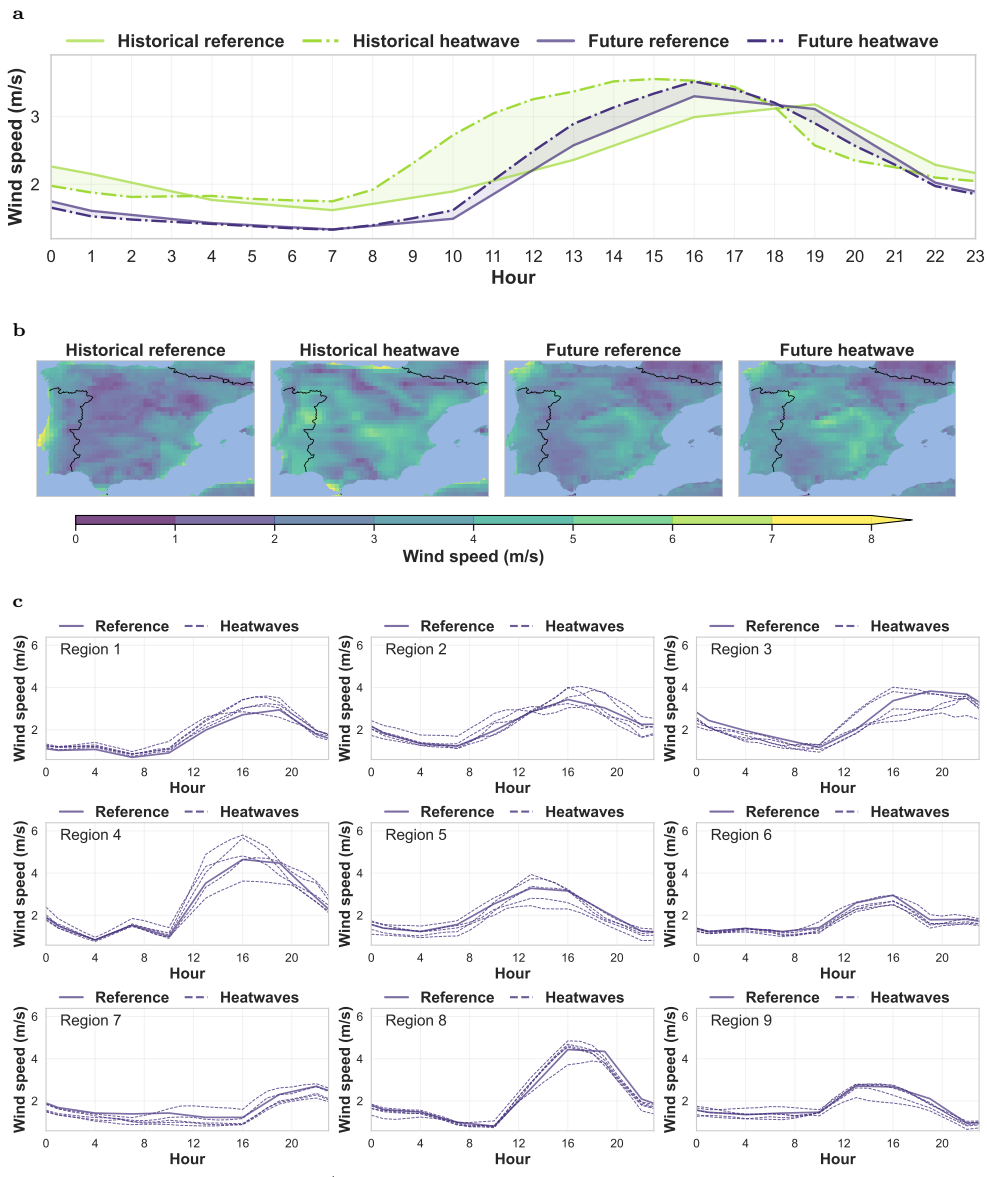
310 For other countries, we provide condensed visualizations in Figures 7 through 13
311 to show the temperature profiles of generated heatwaves.



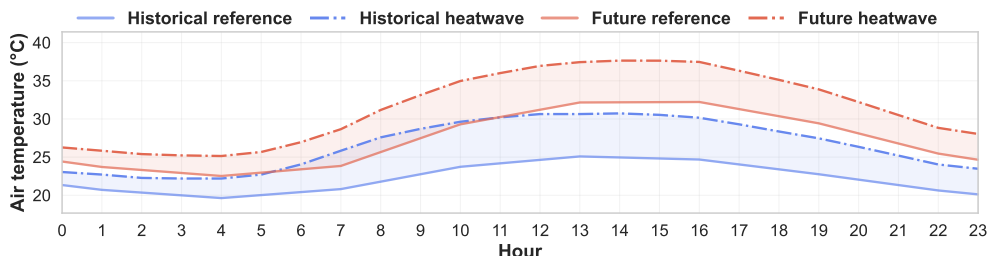
Supplementary Figure 4 | Generated temperature profiles during heatwaves in Spain by 2030 compared to the 2022 records.



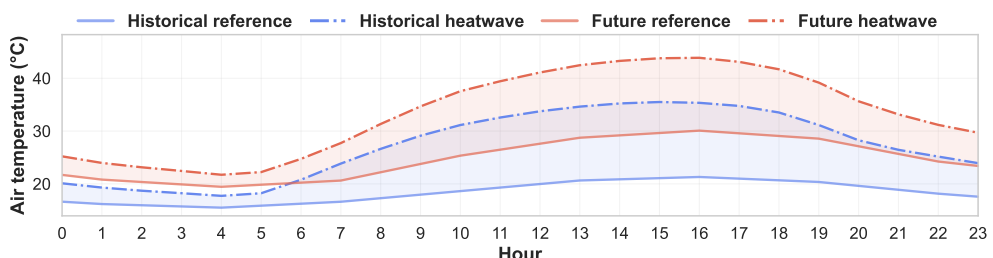
Supplementary Figure 5 | Generated solar radiation profiles during heatwaves in Spain by 2030 compared to the 2022 records.



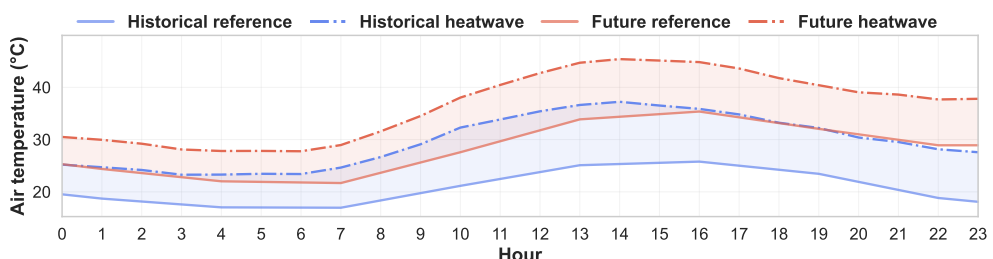
Supplementary Figure 6 | Generated wind speed profiles during heatwaves in Spain by 2030 compared to the 2022 records.



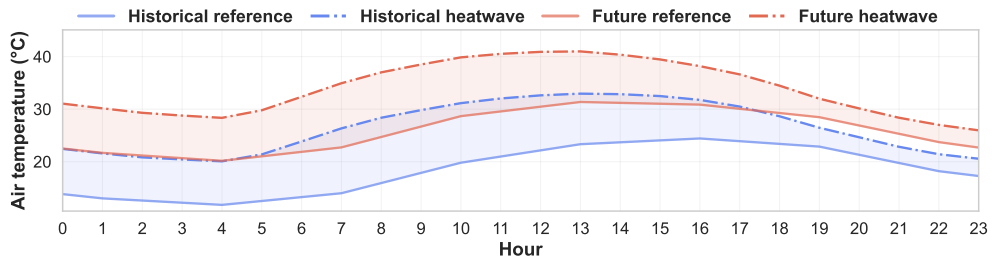
Supplementary Figure 7 | Generated temperature profiles during heatwaves in Italy by 2030 compared to the 2022 records.



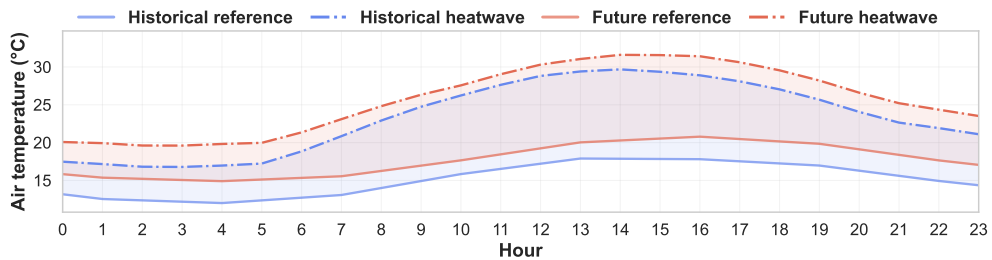
Supplementary Figure 8 | Generated temperature profiles during heatwaves in France by 2030 compared to the 2022 records.



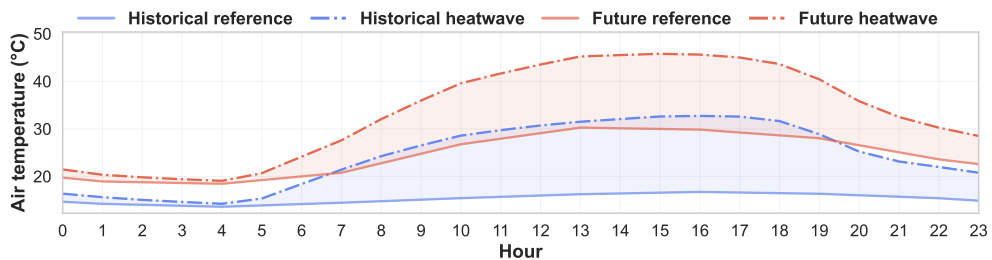
Supplementary Figure 9 | Generated temperature profiles during heatwaves in Portugal by 2030 compared to the 2022 records.



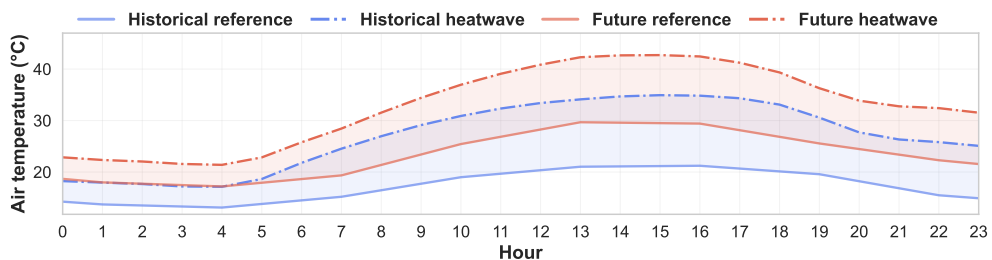
Supplementary Figure 10 | Generated temperature profiles during heatwaves in Germany by 2030 compared to the 2022 records.



Supplementary Figure 11 | Generated temperature profiles during heatwaves in the UK by 2030 compared to the 2019 records.



Supplementary Figure 12 | Generated temperature profiles during heatwaves in Belgium by 2030 compared to the 2022 records.



Supplementary Figure 13 | Generated temperature profiles during heatwaves in the Netherlands by 2030 compared to the 2022 records.

312 **4 EU Simulation Results**

313 **4.1 Setup**

314 Based on generated future weather profiles (2026–2030) derived from the 2019, 2022,
315 and 2024 European heatwaves, we transform renewable generation profiles according
316 to the corresponding weather inputs. We analyze a total of 480 heatwave scenarios
317 per country, comprising **5 years × 24 daily heatwave projections × 4 hottest**
318 **hourly snapshots = 480 scenarios**. Specifically, we select the historically hottest
319 days in June and July in 2019, 2022, and 2024 as heatwave events, then apply the
320 bias-correction methods described in Sec. 3.5 to create future heatwave projections.
321 Load profiles are projected using our calibrated demand model with a baseline annual
322 growth rate of 1% from 2025. For single-snapshot analyses, we set the state of charge
323 (SoC) for storage units to 80% as a baseline setting. Using these baseline parameters,
324 we conduct optimal power flow analysis and model comparison for selected countries.
325 Table 9 provides the detailed model configurations used for comparisons throughout
326 our main manuscript and supplementary information.

327 **Metrics.** To evaluate extreme heatwave impacts on national power grids, we
328 employ three key metrics: (1) **load shedding ratio**, representing unserved load as a
329 percentage of total hourly demand; (2) **line temperature**, calculated via the heat bal-
330 ance equation using current flows from OPF solutions; and (3) **capacity reduction**,
331 computed by as the ratio of thermal-induced line transmission capacity relative to
332 nominal ratings. These metrics collectively quantify grid vulnerability and operational
333 constraints during extreme heat events.

334 We then conduct a **single-country analysis** via OPF for each selected country
335 under projected heatwaves in Sec. 4.2. We also conduct **cross-border analysis** to
336 examine grid interdependencies across multiple countries in Sec. 4.3.

337 **4.2 Heat-flow Analysis for Single Country**

338 We first provide a compact summary of simulation results for eight Western EU coun-
339 tries in Fig. 14, based on the proposed Iter-OPF framework (incorporating thermal
340 modeling for grid analysis and solved using our iterative algorithm). This summary
341 encompasses three key aspects: statistics of temperature and load demand under pro-
342 jected heatwave scenarios; load shedding magnitude and computational running time
343 under the proposed Iter-OPF analysis; and the distribution of line temperatures and
344 associated capacity reductions under projected heatwave conditions.

345 We then present detailed analyses for three countries—Spain, Italy, and France—
346 which exhibit substantial load shedding under projected heatwaves (Figs. 15–23).

347 First, we compare model performance under heatwave scenarios projected from
348 2026 to 2030, generated using a bias-correction approach. We evaluate distributions
349 of line capacity reduction relative to nominal conditions, line temperatures derived
350 from heat balance equations, and load shedding ratios (defined as demand-generation
351 mismatch divided by total demand), alongside average solving times for each scenario.
352 We further examine the relationships between air temperature, load demand, and load
353 shedding ratio across individual simulation scenarios (Figs. 15, 18, 21).

Supplementary Table 9 | Model Baselines for the EU-Grid Simulations.

Models	Conductor model		Generator Derating	Contingency Security Constraint
	Thermal	Segments		
Model Baselines				
AC-OPF	✗	✗	✗	✗
Quad-OPF	quad. approx.	✗	✗	✗
Iter-OPF	✓	✓	✓	✗
TD-OPF	✓	✓	✓	✗
Ablation Study				
w/o thermal	✗	✓	✓	✗
w/o segment	✓	✗	✓	✗
w/o derating	✓	✓	✗	✗
SC-OPF	✗	✗	✗	70%

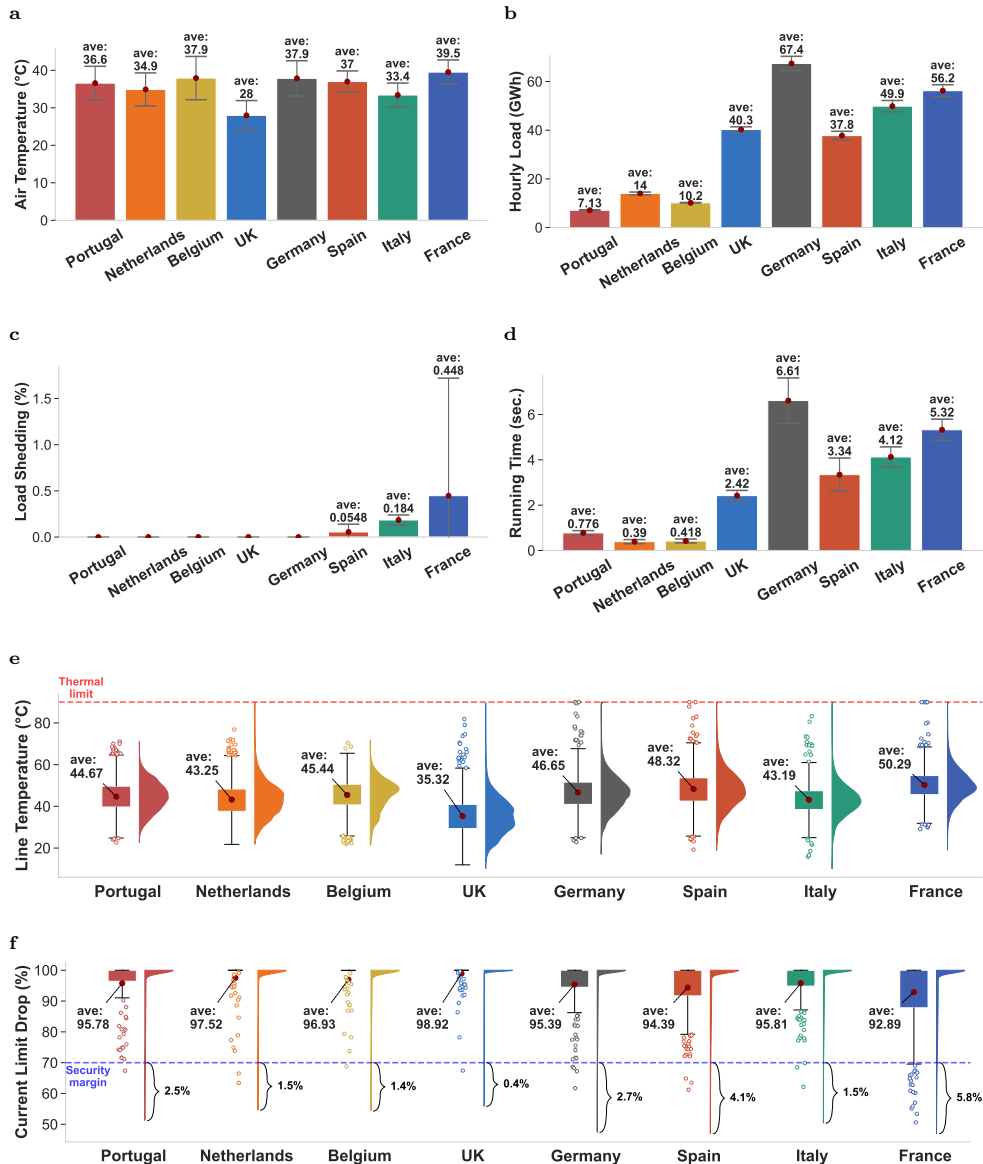
¹ The model baselines include existing and proposed approaches for analyzing grid performance under extreme heatwaves. AC-OPF represents a standard alternating current OPF without heat balance constraints. Quad-OPF applies a quadratic approximation for heat balance and thermal limit constraints. Iter-OPF uses the proposed iterative approach for solving the complete temperature-dependent OPF model. TD-OPF represents the fully converged solution for the exact TD-OPF model.

² The ablation study examines the contribution of individual model components. “w/o thermal” excludes the thermal-dynamic conductor model. “w/o segment” removes line segmentation and uses average weather along the line for thermal modeling. “w/o derating” omits generator derating factors. SC-OPF incorporates a 70% security constraint margin without thermal modeling.

Second, we analyze the spatiotemporal evolution of grid thermal stress and load shedding across diurnal and interannual scales. We track line capacity reduction and transmission line temperature variations across different times of day and projection years, benchmarked against the 70% security margin and the 90°C thermal limit, respectively. We also visualize the spatial distribution of air temperature and transmission line temperature during peak afternoon hours (12:00–15:00) for representative heatwave scenarios in 2030 (Figs. 16, 19, 22).

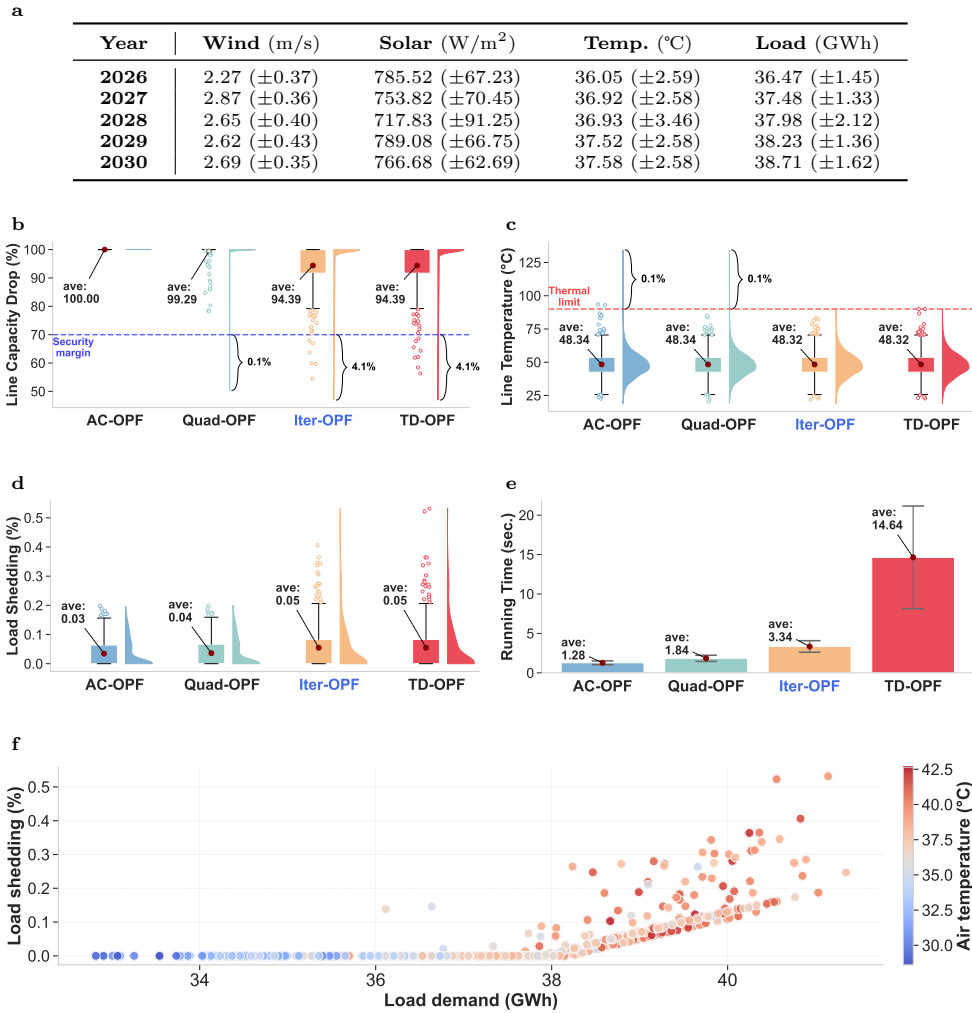
Third, we conduct ablation studies to quantify the impact of removing individual modeling components from the iterative optimal power flow framework, benchmarking against the security-constrained optimal power flow method with a 70% security margin [1]. We further assess sensitivity to different physical thermal models—comparing individual conductor formulations with corrected models that account for bundle effects—and examine thermal limit assumptions ranging from 90°C to 180°C. Finally, we evaluate how varying annual load growth rates (1%–3%) and initial battery state-of-charge levels (0%–100%) influence load shedding outcomes (Figs. 17, 20, 23).

Key observations include the following. (i) Existing optimal power flow models substantially overestimate grid resilience during heatwaves, underscoring the need for temperature-dependent formulations. (ii) Complete thermal modeling is essential for accurate resilience assessment, as simplified approaches fail to capture critical thermal constraints. (iii) Rising demand amplifies grid stress, yet energy storage alone provides limited relief, suggesting that infrastructure upgrades and demand-side management must complement storage deployment. (iv) Grid vulnerability differs substantially by country, reflecting variations in network topology, generation mix, and climatic exposure.

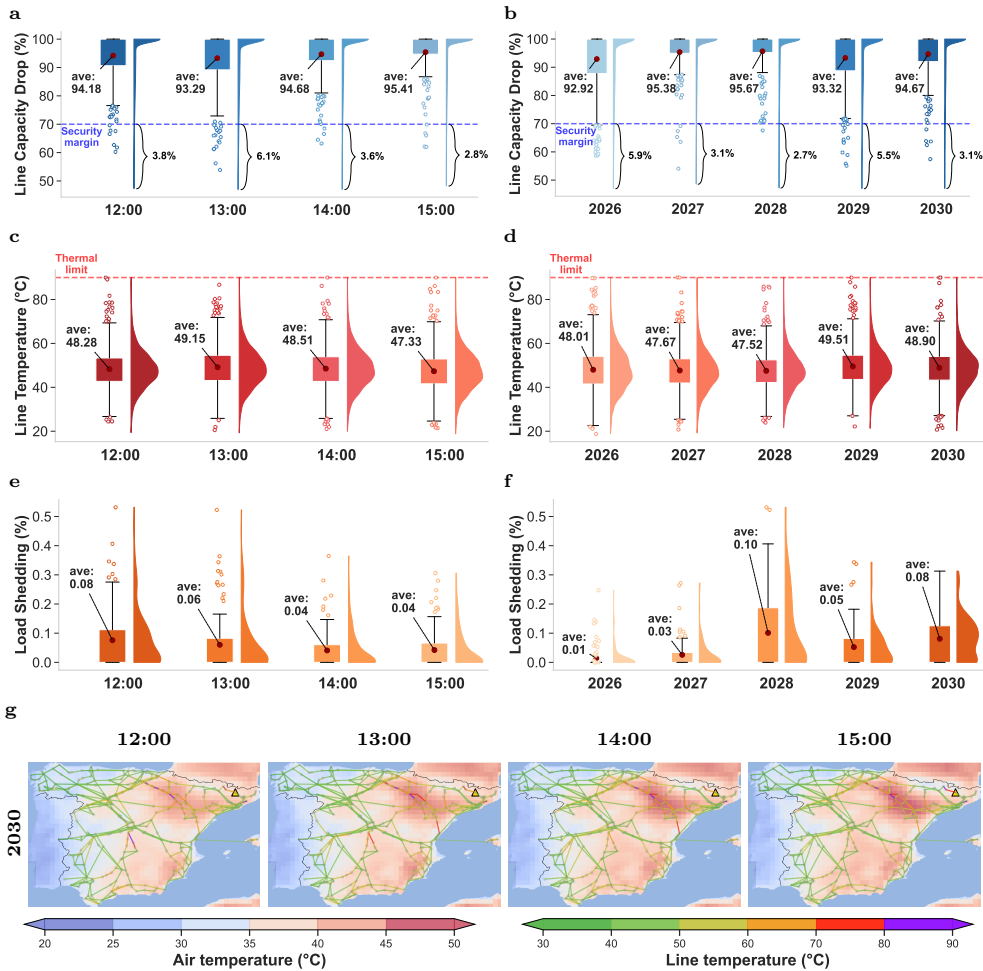


Supplementary Figure 14 | National grids in Western Europe, such as France, Italy, and Spain, exhibit substantial load shedding under projected heatwaves, while other countries remain resilient. **a** Average air temperature during the hottest hours in projected heatwave periods. **b** Average hourly load demand for heatwave scenarios estimated by calibrated demand models. **c** Average load shedding across different countries. **d** Average running time per scenario for different national grids. **e** Distribution of line temperature under OPF analysis with projected heatwaves. **f** Distribution of line capacity reduction compared to nominal ratings during heatwaves. Average values and percentages above/below thresholds are indicated.

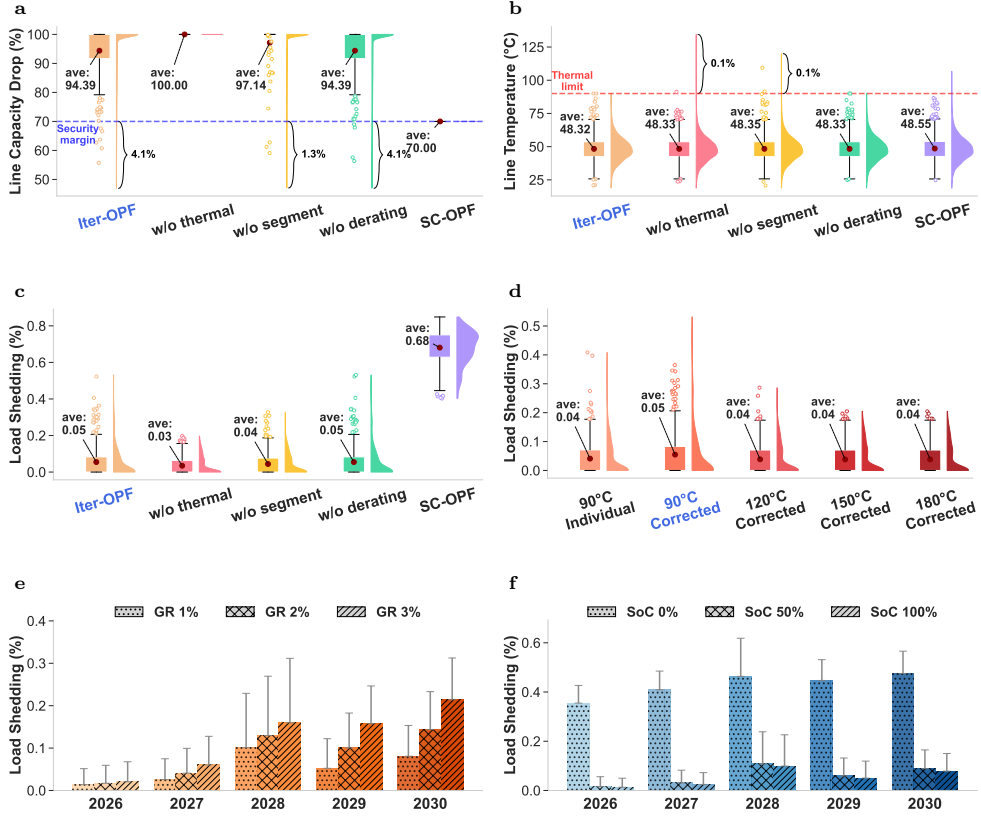
4.2.1 Spain



Supplementary Figure 15 | OPF analysis comparison in Spanish Grid. **a** Weather and load statistics under heatwave projections from 2026 to 2030, with 480 scenarios generated using a bias-correction approach. **b–c** Distributions of estimated line capacity reduction relative to nominal conditions and line temperatures derived from heat balance equations. Box plots display the average value (center point), interquartile range (box), and $1.5 \times$ interquartile range (whiskers); violin plots show the probability density distribution. Average values and percentages above/below thresholds are indicated. **d** Distributions of load shedding ratios (demand-generation mismatch divided by total demand). **e** Average per-scenario solving times. **f** Relationships between air temperature, load demand, and load shedding ratio; each point represents a single simulation scenario.

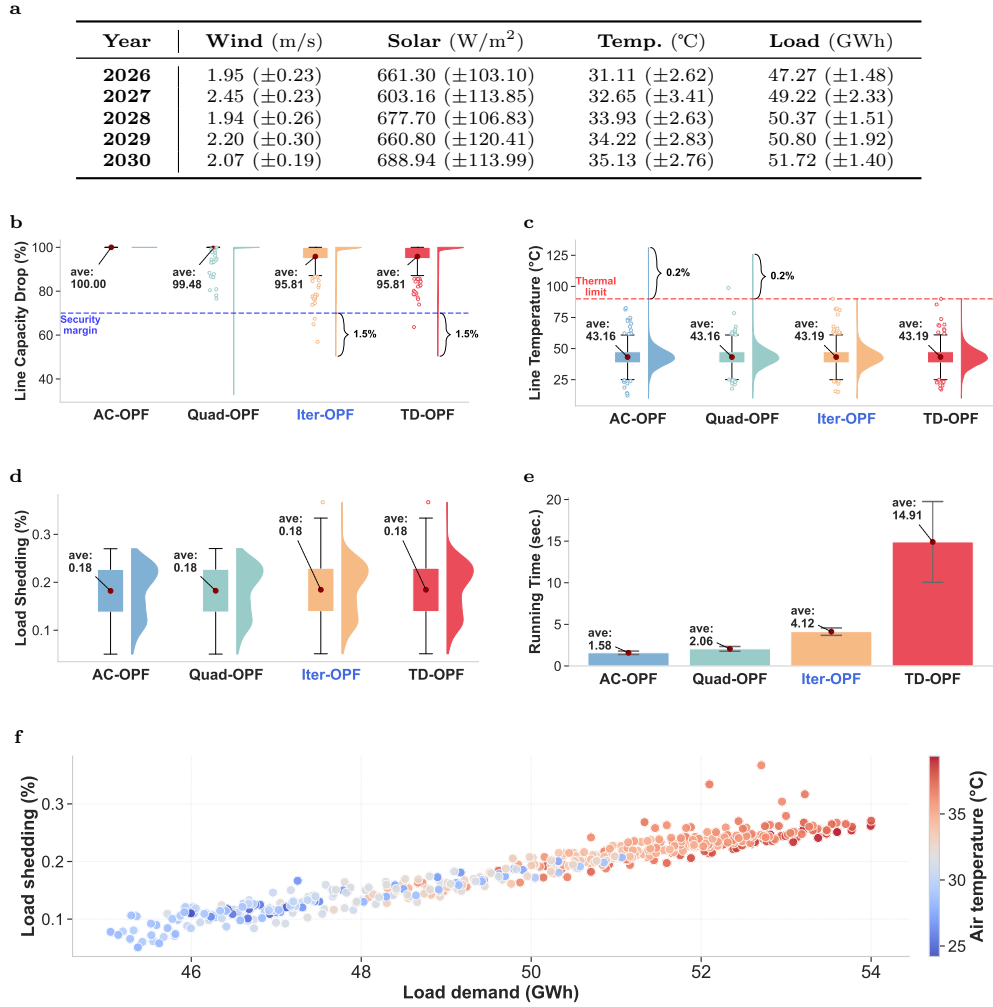


Supplementary Figure 16 | Spatiotemporal evolution of grid thermal stress and load shedding under heatwave conditions across diurnal and inter-annual scales. **a–b** Line capacity reduction across different times of day (**a**) and projection years (**b**); the dashed blue line indicates the 70% security margin. **c–d** Transmission line temperature variations across hours of day (**c**) and projection years (**d**); the dashed red line indicates the 90°C thermal limit. **e–f** Distribution of load shedding ratios across hours of day (**e**) and projection year (**f**). **g** Power grid visualisation showing the spatial distribution of air temperature (background shading; darker red indicates higher temperatures) and transmission line temperature (network overlay; red and purple indicate proximity to thermal limits) during peak afternoon hours (12:00–15:00) for a representative heatwave scenario in 2030. Yellow triangles (\blacktriangle) denote buses experiencing load shedding.

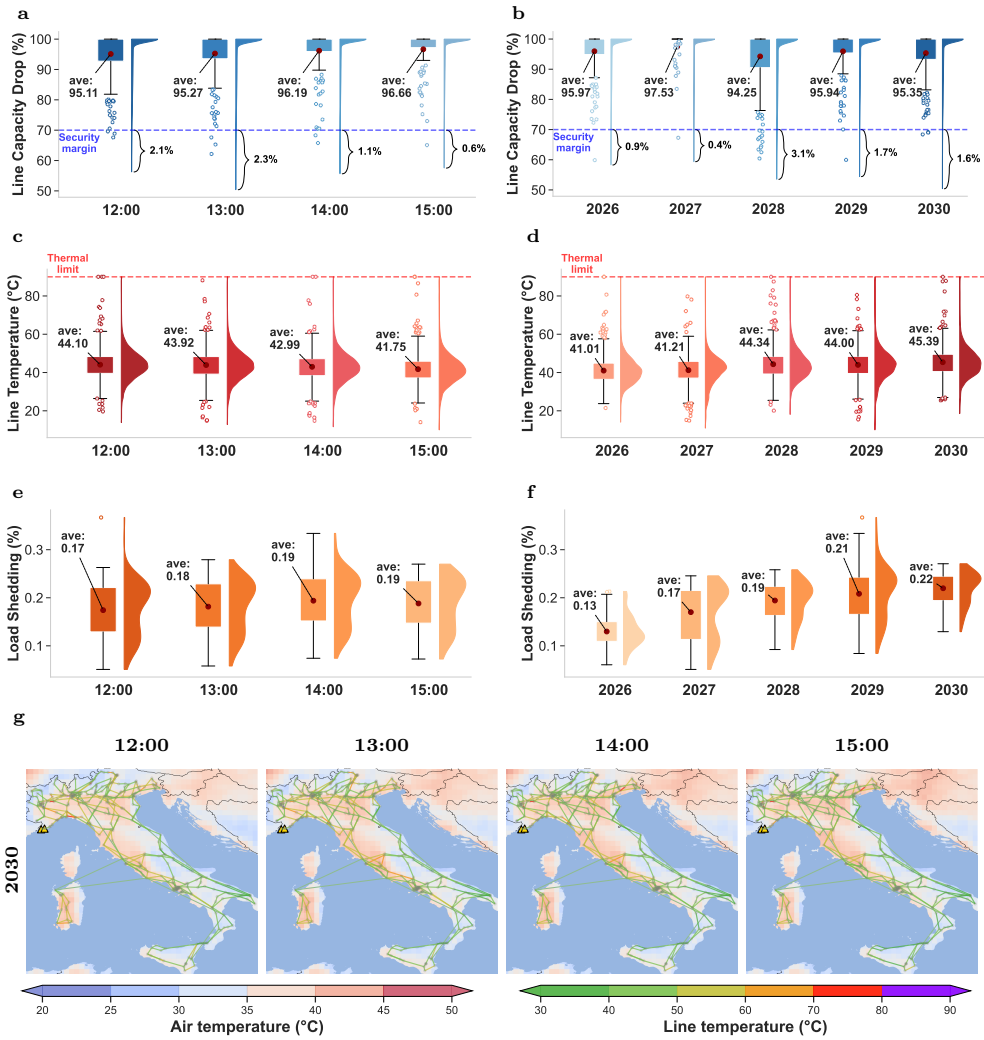


Supplementary Figure 17 | Ablation study of thermal modeling, impacts of the physical thermal model, and sensitivity to load growth and storage conditions under heatwave scenarios. **a–c** Impact of removing different modeling components from the Iter-OPF framework on capacity reduction (a), line temperatures (b), and load shedding ratios (c), compared to the 70% security margin SC-OPF method. **d** Sensitivity of load shedding to different physical thermal models (detailed in Sec. 3.4) and thermal limit assumptions (individual conductor model at 90°C versus corrected model with thermal ratings at 90°C, 120°C, 150°C, and 180°C). Note that high thermal limits reduce the formulation into AC-OPF with derated generation. **e–f** Sensitivity analysis of load shedding ratios under varying annual load growth rates (GR: 1%, 2%, and 3%) (e) and initial battery state-of-charge levels (SoC: 0%, 50%, and 100%) (f). Box plots display the average value (center point), interquartile range (box), and 1.5× interquartile range (whiskers); violin plots show the probability density distribution.

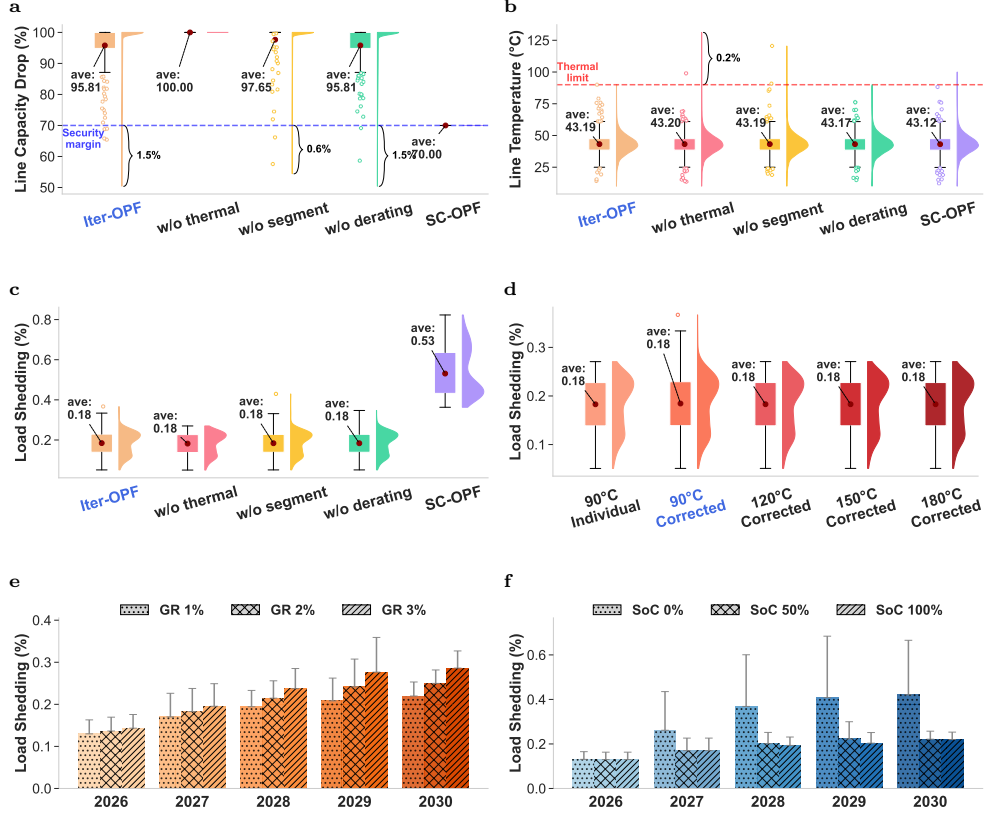
4.2.2 Italy



Supplementary Figure 18 | OPF analysis comparison in Italian Grid. **a** Weather and load statistics under heatwave projections from 2026 to 2030, with 480 scenarios generated using a bias-correction approach. **b–c** Distributions of estimated line capacity reduction relative to nominal conditions and line temperatures derived from heat balance equations. Box plots display the average value (center point), interquartile range (box), and 1.5× interquartile range (whiskers); violin plots show the probability density distribution. **d** Distributions of load shedding ratios (demand-generation mismatch divided by total demand). **e** Average per-scenario solving times. **f** Relationships between air temperature, load demand, and load shedding ratio; each point represents a single simulation scenario.

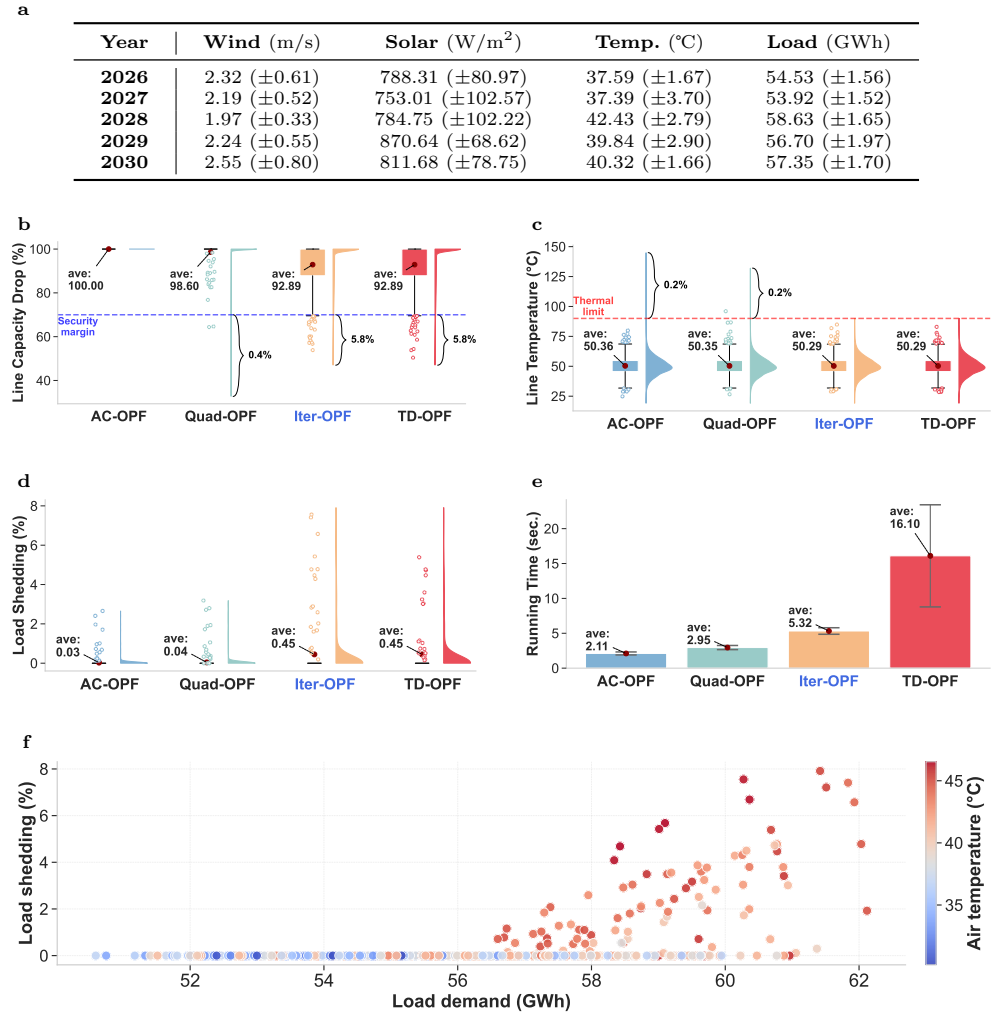


Supplementary Figure 19 | Spatiotemporal evolution of grid thermal stress and load shedding under heatwave conditions across diurnal and inter-annual scales. **a–b** Line capacity reduction across different times of day (**a**) and projection years (**b**); the dashed blue line indicates the 70% security margin. **c–d** Transmission line temperature variations across hours of day (**c**) and projection years (**d**); the dashed red line indicates the 90°C thermal limit. **e–f** Distribution of load shedding ratios across hours of day (**e**) and projection year (**f**). **g** Power grid visualisation showing the spatial distribution of air temperature (background shading; darker red indicates higher temperatures) and transmission line temperature (network overlay; red and purple indicate proximity to thermal limits) during peak afternoon hours (12:00–15:00) for a representative heatwave scenario in 2030. Yellow triangles (Δ) indicate buses experiencing load shedding.

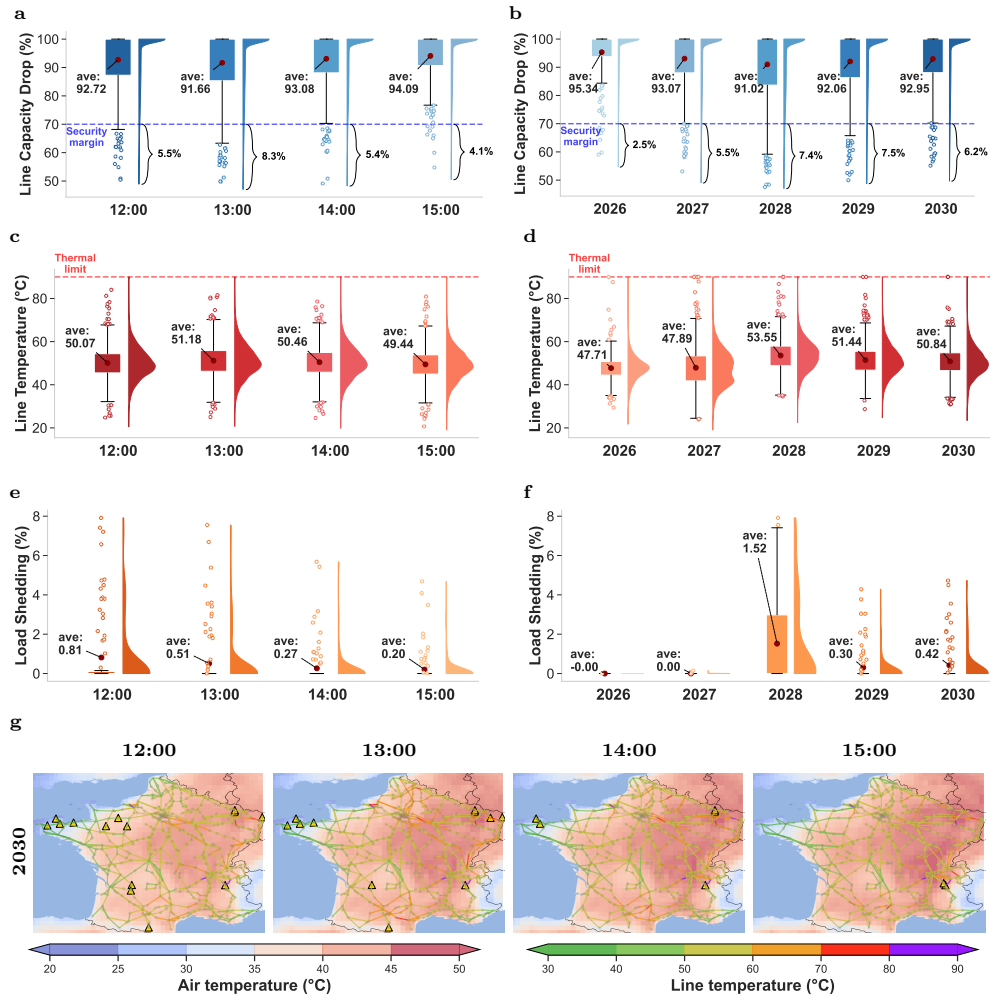


Supplementary Figure 20 | Ablation study of thermal modeling, impacts of the physical thermal model, and sensitivity to load growth and storage conditions under heatwave scenarios. **a–c** Impact of removing different modeling components from the Iter-OPF framework on capacity reduction (a), line temperatures (b), and load shedding ratios (c), compared to the 70% security margin SC-OPF method. **d** Sensitivity of load shedding to different physical thermal models (detailed in Sec. 3.4) and thermal limit assumptions (individual conductor model at 90°C versus corrected model with thermal ratings at 90°C, 120°C, 150°C, and 180°C). Note that high thermal limits reduce the formulation into AC-OPF with derated generation. **e–f** Sensitivity analysis of load shedding ratios under varying annual load growth rates (GR: 1%, 2%, and 3%) (e) and initial battery state-of-charge levels (SoC: 0%, 50%, and 100%) (f). Box plots display the average value (center point), interquartile range (box), and 1.5× interquartile range (whiskers); violin plots show the probability density distribution.

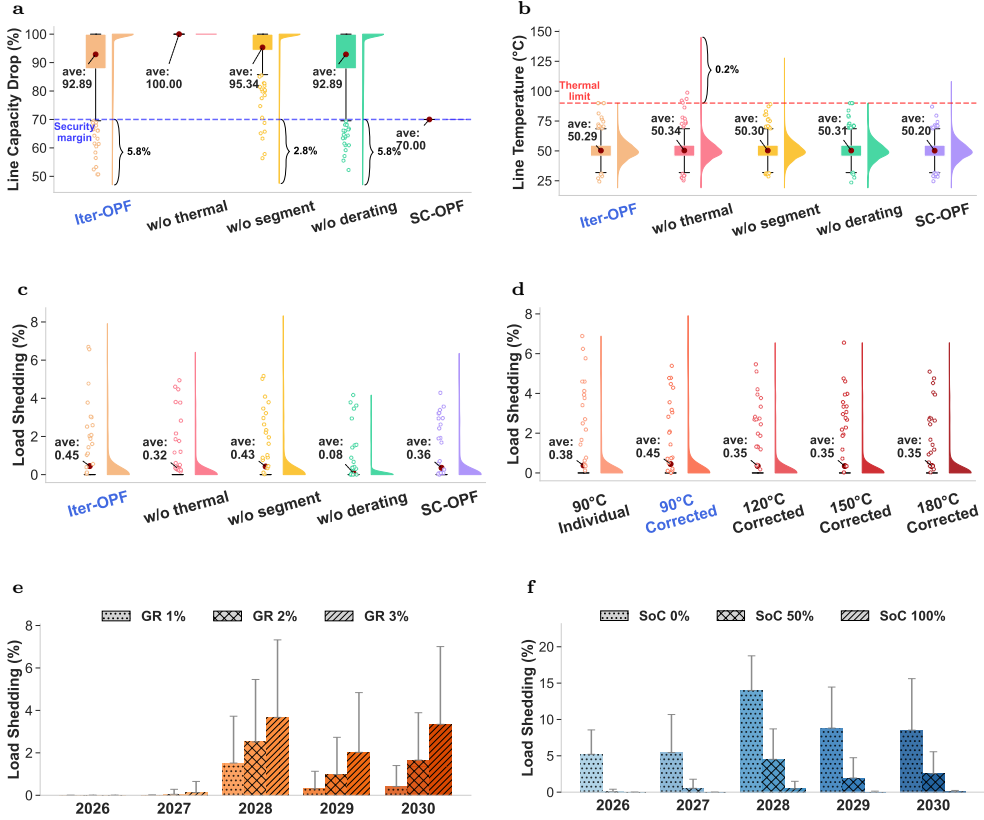
4.2.3 France



Supplementary Figure 21 | OPF analysis comparison in French Grid. **a** Weather and load statistics under heatwave projections from 2026 to 2030, with 480 scenarios generated using a bias-correction approach. **b–c** Distributions of estimated line capacity reduction relative to nominal conditions and line temperatures derived from heat balance equations. Box plots display the average value (center point), interquartile range (box), and $1.5 \times$ interquartile range (whiskers); violin plots show the probability density distribution. **d** Distributions of load shedding ratios (demand-generation mismatch divided by total demand). **e** Average per-scenario solving times. **f** Relationships between air temperature, load demand, and load shedding ratio; each point represents a single simulation scenario.



Supplementary Figure 22 | Spatiotemporal evolution of grid thermal stress and load shedding under heatwave conditions across diurnal and inter-annual scales. **a–b** Line capacity reduction across different times of day (a) and projection years (b); the dashed blue line indicates the 70% security margin. **c–d** Transmission line temperature variations across hours of day (c) and projection years (d); the dashed red line indicates the 90°C thermal limit. **e–f** Distribution of load shedding ratios across hours of day (e) and projection year (f). **g** Power grid visualisation showing the spatial distribution of air temperature (background shading; darker red indicates higher temperatures) and transmission line temperature (network overlay; red and purple indicate proximity to thermal limits) during peak afternoon hours (12:00–15:00) for a representative heatwave scenario in 2030. Yellow triangles (Δ) indicate buses experiencing load shedding.



Supplementary Figure 23 | Ablation study of thermal modeling, impacts of the physical thermal model, and sensitivity to load growth and storage conditions under heatwave scenarios. **a–c** Impact of removing different modeling components from the Iter-OPF framework on capacity reduction (a), line temperatures (b), and load shedding ratios (c), compared to the 70% security margin SC-OPF method. **d** Sensitivity of load shedding to different physical thermal models (detailed in Sec. 3.4) and thermal limit assumptions (individual conductor model at 90°C versus corrected model with thermal ratings at 90°C, 120°C, 150°C, and 180°C). Note that high thermal limits reduce the formulation into AC-OPF with derated generation. **e–f** Sensitivity analysis of load shedding ratios under varying annual load growth rates (GR: 1%, 2%, and 3%) (e) and initial battery state-of-charge levels (SoC: 0%, 50%, and 100%) (f). Box plots display the average value (center point), interquartile range (box), and 1.5× interquartile range (whiskers); violin plots show the probability density distribution.

378 **4.3 Cross-Border Analysis for Multiple Countries**

379 We conduct cross-border analysis to examine grid interdependencies across multi-
380 ple European countries. By simulating national grids both in isolation and jointly
381 with neighboring countries under identical heatwave scenarios, we quantify how
382 international interconnections influence key resilience metrics.

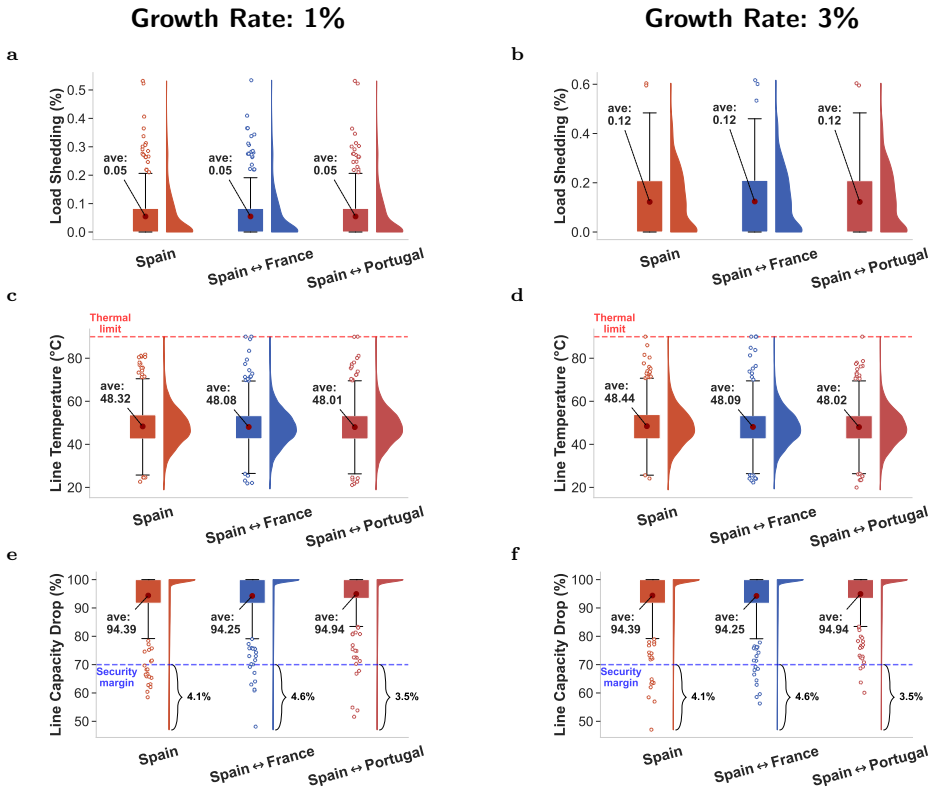
383 Our analysis reveals asymmetries in how cross-border interconnections affect grid
384 resilience across different national contexts.

385 For Spain, cross-border interconnections provide no substantial relief for grid
386 capacity bottlenecks during heatwaves (Fig. 24). We compare single-country analyses
387 with joint multi-country configurations—including Spain–Portugal and Spain–France
388 pairings—under identical heatwave projections from 2026 to 2030. Across both 1% and
389 3% annual load growth scenarios, the distributions of load shedding ratios, line temper-
390 atures, and capacity reductions remain largely unchanged regardless of interconnection
391 configuration. This finding indicates that Spanish grid vulnerabilities are predom-
392inantly driven by internal transmission constraints rather than limited import capacity.
393 Spatial visualization of grid thermal stress during peak heatwave conditions confirms
394 this interpretation (Fig. 25): transmission lines approaching the 90°C thermal limit
395 and buses experiencing load shedding are concentrated within the Spanish interior,
396 with minimal alleviation observed when cross-border flows from Portugal or France are
397 enabled. Even under the more aggressive 3% load growth scenario, interconnections
398 fail to meaningfully reduce thermal stress on critical domestic corridors.

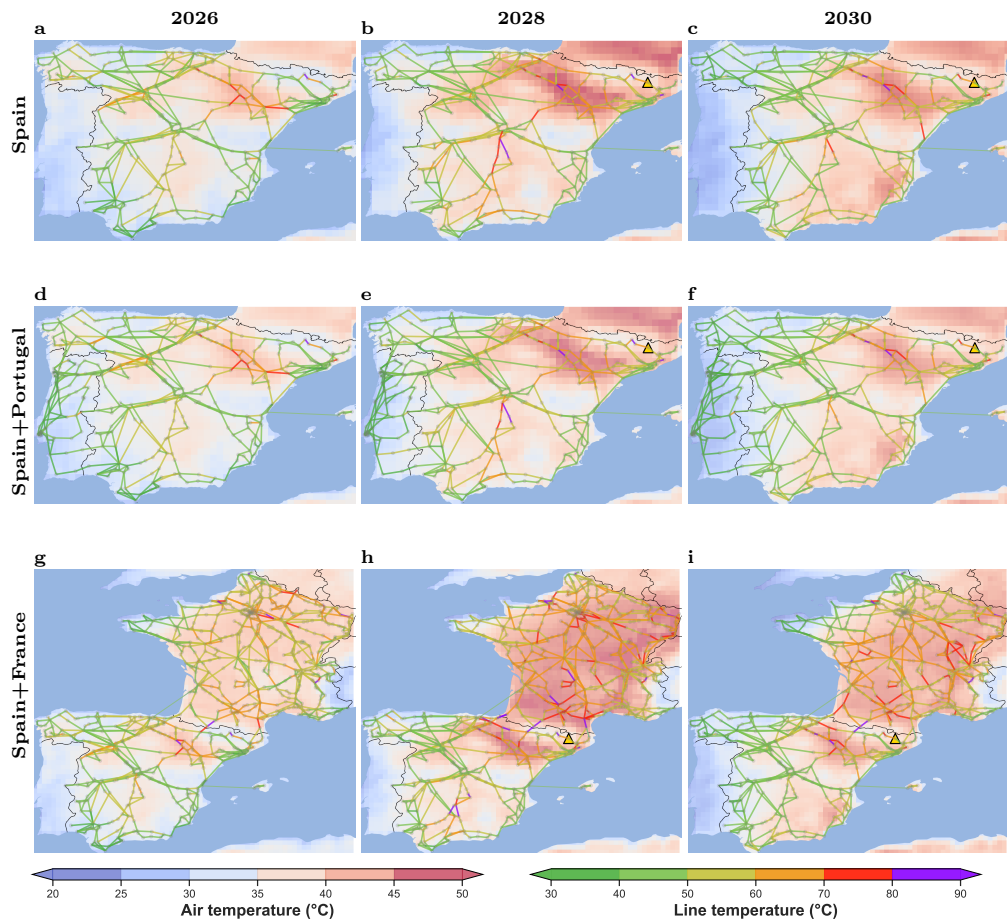
399 In contrast, cross-border interconnections provide substantial relief for French
400 grid capacity bottlenecks during heatwaves (Fig. 26). Under identical heatwave con-
401 ditions, joint multi-country simulations yield markedly lower load shedding ratios
402 compared to France-only scenarios, with benefits persisting across both 1% and 3%
403 load growth assumptions. Line temperatures and capacity reductions similarly improve
404 when interconnections with neighboring countries are activated, as confirmed by spa-
405 tial visualization of thermal stress during peak conditions (Fig. 27). This divergence
406 from the Spanish case reflects fundamental differences in network topology and the spa-
407 tial distribution of generation assets relative to demand centers. France benefits from
408 a more meshed transmission network and stronger interconnection capacity, enabling
409 effective load balancing through cross-border power exchanges during periods of peak
410 thermal stress.

411 These contrasting outcomes carry important implications for European grid plan-
412 ning and climate adaptation. While interconnection expansion is frequently advocated
413 as a pathway to enhanced resilience, our results demonstrate that its effective-
414 ness is highly context-dependent. Countries facing binding internal transmis-
415 sion constraints—such as Spain—may derive limited benefit from increased cross-border
416 capacity without concurrent investment in domestic network reinforcement. Con-
417 versely, countries with adequate internal transmission headroom—such as France—can
418 leverage interconnections to substantially mitigate heatwave-induced grid stress. These
419 findings underscore the need for nationally tailored adaptation strategies that account
420 for the unique combination of network topology, generation portfolio, and climatic
421 exposure in each country.

422 4.3.1 Spain and Neighboring Countries

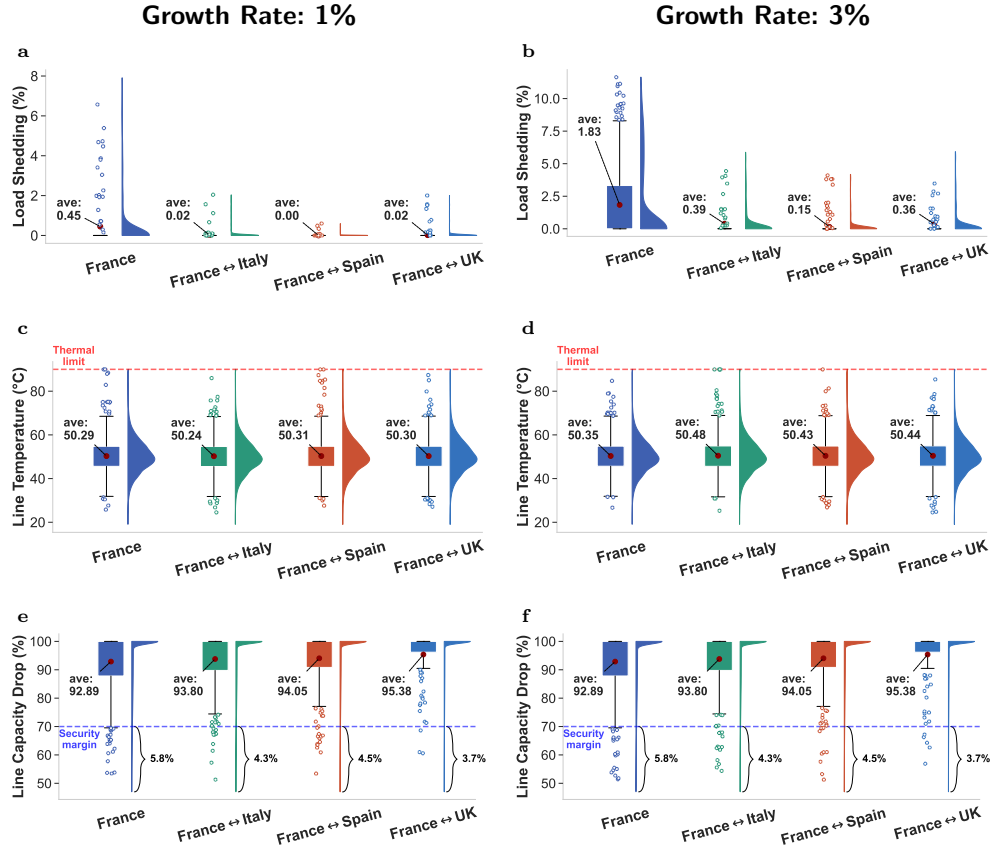


Supplementary Figure 24 | Cross-border interconnections provide no substantial relief for Spanish grid capacity bottlenecks during heatwaves. We compare single-country analyses with joint multi-country analyses for the Spanish grid under identical heatwave projections to quantify the effects of cross-border interconnections on grid resilience. **a–b** Distribution of load shedding ratios in Spain across different interconnection scenarios under 1% (**a**) and 3% (**b**) annual load growth rates. **c–d** Distribution of line temperatures in Spain across different interconnection scenarios under 1% (**c**) and 3% (**d**) annual load growth rates. **e–f** Distribution of line capacity reductions in Spain across different interconnection scenarios under 1% (**e**) and 3% (**f**) annual load growth rates. Box plots display the average value (center point), interquartile range (box), and $1.5 \times$ interquartile range (whiskers); violin plots show the probability density distribution.

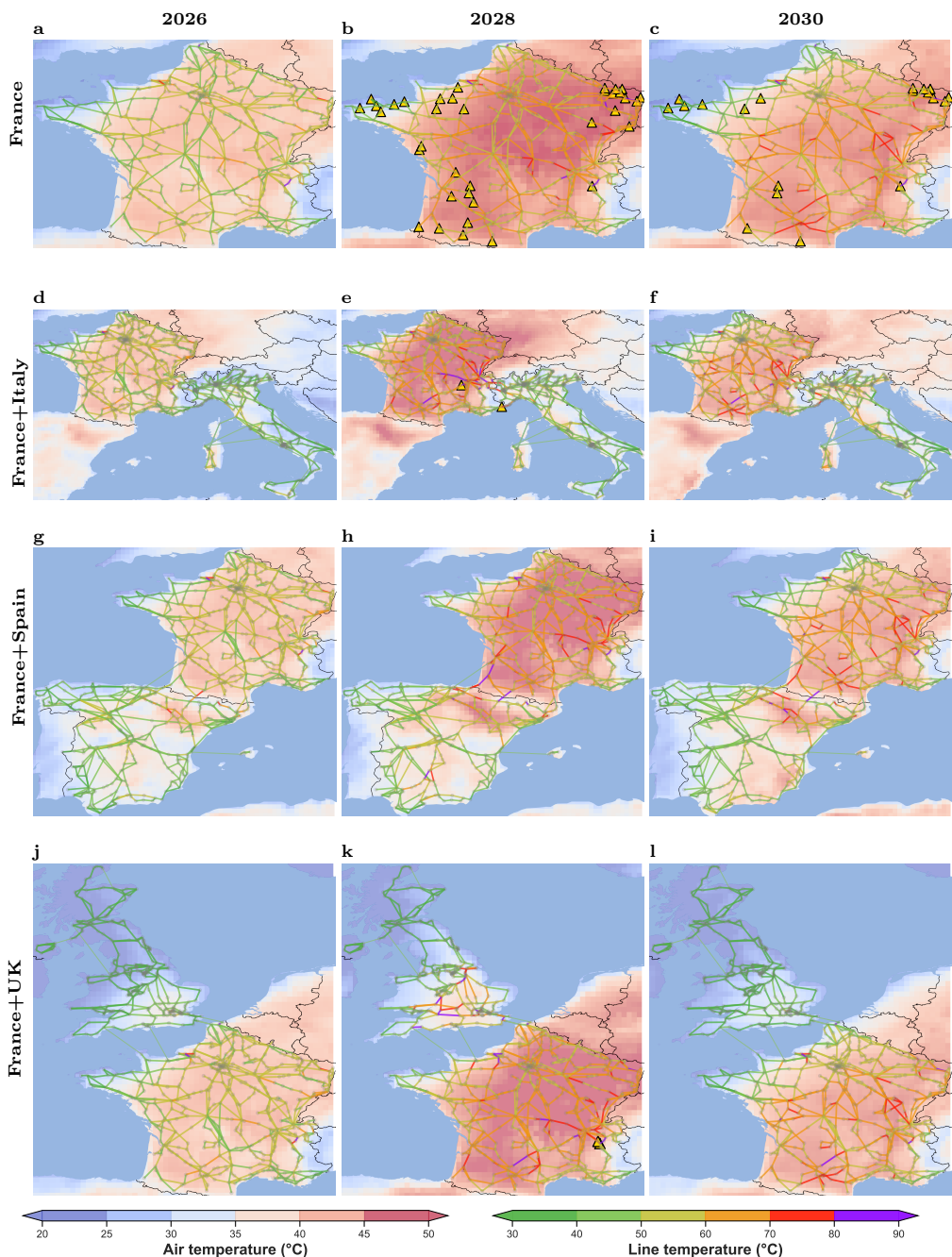


Supplementary Figure 25 | Cross-border analysis for Spain, Portugal, and France under baseline settings. Spatial distribution of air temperature (background shading) and transmission line temperature (network overlay) during peak heatwave conditions for 2026, 2028, and 2030 under a 1% annual load growth rate and 80% initial storage state of charge. **a–c**, Spain-only analysis. **d–f**, Spain–Portugal joint analysis. **g–i**, Spain–France joint analysis. Yellow triangles denote buses experiencing load shedding. Line colours indicate conductor temperature, with red and purple indicating proximity to the 90°C thermal limit.

423 **4.3.2 France and Neighboring Countries**



Supplementary Figure 26 | Cross-border interconnections provide substantial relief for French grid capacity bottlenecks during heatwaves. We compare single-country analyses with joint multi-country analyses for the Spanish grid under identical heatwave projections to quantify the effects of cross-border interconnections on grid resilience. **a–b** Distribution of load shedding ratios in Spain across different interconnection scenarios under 1% (**a**) and 3% (**b**) annual load growth rates. **c–d** Distribution of line temperatures in Spain across different interconnection scenarios under 1% (**c**) and 3% (**d**) annual load growth rates. **e–f** Distribution of line capacity reductions in Spain across different interconnection scenarios under 1% (**e**) and 3% (**f**) annual load growth rates. Box plots display the average value (center point), interquartile range (box), and $1.5 \times$ interquartile range (whiskers); violin plots show the probability density distribution.



Supplementary Figure 27 | Cross-border analysis for France, Italy, Spain, and the UK under baseline settings. French distribution of air temperature (background shading) and transmission line temperature (network overlay) during peak heatwave conditions for 2026, 2028, and 2030 under a 1% annual load growth rate and 80% initial storage state of charge.

5 IEEE Benchmark Simulation

We use the IEEE 30-bus system as a benchmark to evaluate the effectiveness of our proposed methodology. This system comprises 30 nodes ($|\mathcal{N}| = 30$), 6 generators ($|\mathcal{G}| = 6$), 41 transmission lines ($|\mathcal{L}| = 41$), and 12 contingency scenarios ($|\mathcal{C}| = 12$). The number of contingency scenarios is fewer than the total number of transmission lines due to network connectivity constraints.

Our implementation adopts transmission line conductor specifications outlined in IEEE standards [33]. Security constraints are implemented using a preventive approach [34], in which real power generation dispatch at non-slack buses remains fixed across all post-contingency scenarios, while other control variables (such as reactive power and voltage magnitudes) may be adjusted in response to contingencies.

As shown in Table 10, we conduct a comparative analysis of multiple model formulations: the baseline model (AC-OPF), a temperature-dependent model with quadratic approximation of thermal constraints [35] (Quad-OPF), our proposed iterative approach (Iter-OPF), and the fully converged temperature-dependent OPF solution (TD-OPF). We also evaluate ablated variants of the iterative approach (Iter-OPF), excluding either thermal modeling (w/o thermal) or derating modeling (w/o derating). Additionally, we compare our thermal-based modeling approach against security-constrained AC-OPF formulations (detailed in Sec. 2.2), including AC-SC-OPF, the complete $N-1$ AC-based security-constrained formulation; DC-SC-OPF, AC-OPF with security margins approximated via line outage distribution factors [12]; and fixed-SC-OPF, AC-OPF with a fixed 70% security margin [1].

We note that several studies employ DC-OPF-based formulations incorporating weather-dependent dynamic line rating approaches [18]. However, these DC models are not AC-feasible due to their linear simplifications and fail to capture the coupling effects between power flow and heat transfer. Accordingly, we consider only AC-based models in our evaluation.

Supplementary Table 10 | Model Baselines for the IEEE-30 Simulations.

Models	Conductor model Thermal	Generator Derating	Contingency Security Constraint
Models Baselines			
AC-OPF	✗	✗	✗
Quad-OPF	quad. approx.	✗	✗
Iter-OPF	✓	✓	✓
TD-OPF	✓	✓	✓
Sensitivity Analysis			
w/o thermal	✗	✓	✓
w/o derating	✓	✗	✓
AC-SC-OPF	✗	✗	Exact
DC-SC-OPF	✗	✗	Linear
Fix-SC-OPF	✗	✗	Fixed

451 **Thermal Modeling is Essential for Grid Resilience Assessment**

452 We compare model performance at a 0.9 load ratio across different weather profiles
453 (Fig. 28): mild conditions (0.61m/s wind speed, 25°C ambient temperature) [33] and
454 extreme conditions (0.1 m/s wind speed, 45°C ambient temperature).

455 Under mild weather conditions, AC-OPF, Quad-OPF, Iter-OPF, and TD-OPF
456 all achieve zero load shedding while maintaining thermal feasibility. Under extreme
457 weather conditions, the thermal-aware formulations (Iter-OPF and TD-OPF) increase
458 load shedding to 8.06%, reflecting reduced line ampacity at elevated temperatures.
459 In contrast, AC-OPF maintains zero load shedding but produces thermal violations
460 exceeding 90°C—an operationally infeasible outcome. Quad-OPF exhibits lower
461 load shedding due to its quadratic approximation, which permits slight temperature
462 exceedances, representing a potentially unsafe operating regime.

463 Ablation studies confirm the necessity of both modeling components. Removing
464 thermal modeling leads to underestimated line temperatures and undetected violations,
465 while removing derating modeling yields 7.09% load shedding—demonstrating
466 that accurate capacity derating is essential for reliable dispatch. Notably, Iter-OPF
467 achieves comparable solution quality to TD-OPF with substantially reduced computa-
468 tion time (0.42s versus 1.03s), making it suitable for operational planning/assessment
469 applications.

470 **Security Constraints Cause Excessive Curtailment Under
471 Normal Conditions and Insufficient Protection Under Stress**

472 Security-constrained formulations impose weather-independent capacity margins that
473 fail to adapt to actual operating conditions (Fig. 28). AC-SC-OPF requires 7.29% load
474 shedding, DC-SC-OPF requires 6.33%, and Fixed-SC-OPF requires 4.18%—regardless
475 of prevailing weather. These static margins cause unnecessary curtailment under mild
476 conditions while still permitting thermal violations during extreme events.

477 Our thermal-aware formulation addresses this limitation by dynamically adjusting
478 transmission capacity based on electrothermal interactions. This approach maximizes
479 asset utilization under favorable conditions while ensuring adequate protection during
480 thermal stress. The contrast highlights a fundamental shortcoming of conventional
481 security-constrained approaches: by treating all weather conditions identically, they
482 sacrifice efficiency without guaranteeing safety.

483 These findings underscore the importance of comprehensive electrothermal mod-
484 eling that captures the complex interactions among ambient conditions, transmission
485 line thermal behavior, and generation dispatch. As climate change increases the
486 frequency and severity of extreme weather events, physics-based thermal modeling
487 becomes increasingly critical for ensuring grid resilience.

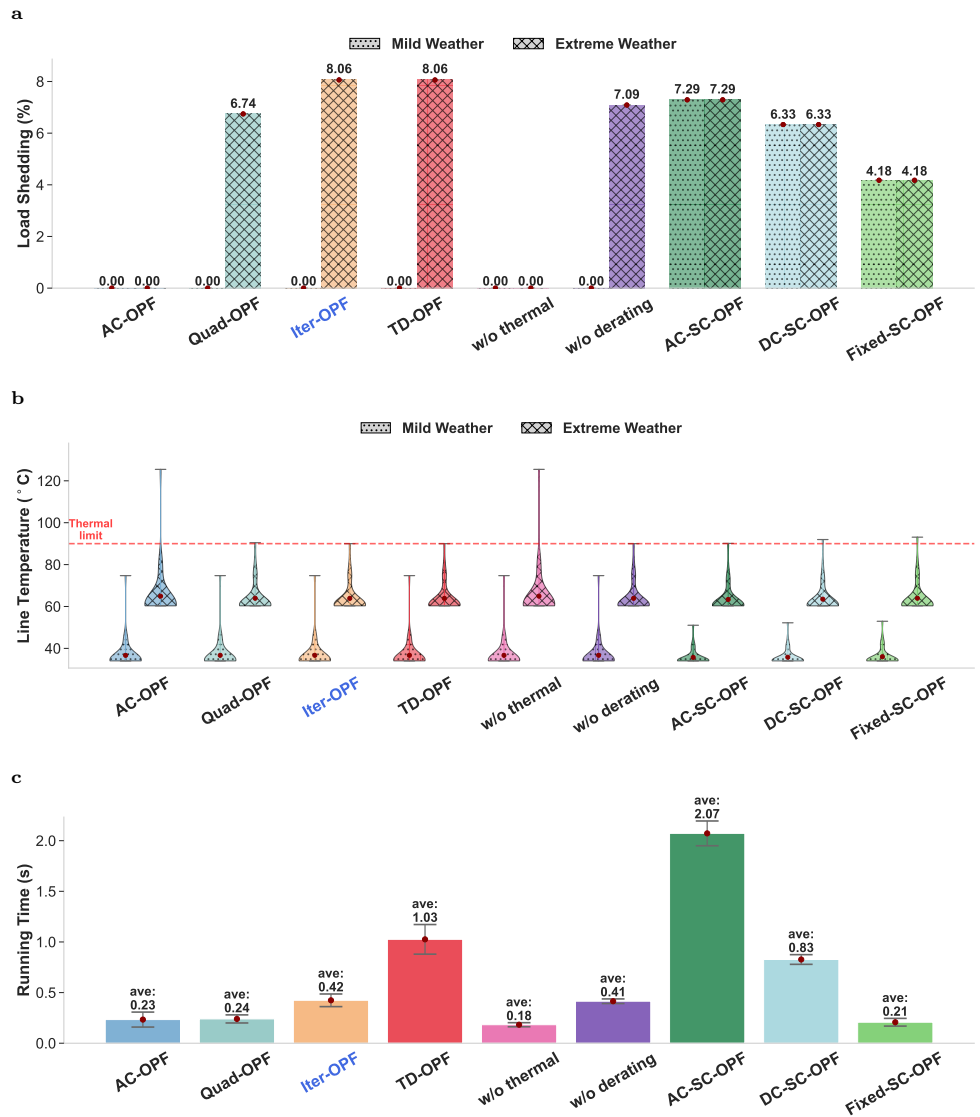
488 **Compound Effects of Extreme Weather: High Temperature
489 and Low Wind**

490 We examine model performance under four weather scenarios—mild (0.61m/s, 25°C),
491 low-wind (0.1m/s, 25°C), high-temperature (0.61m/s, 45°C), and extreme (0.1m/s,
492 45°C)—at load ratios of 0.9 and 1.0 (Fig. 29).

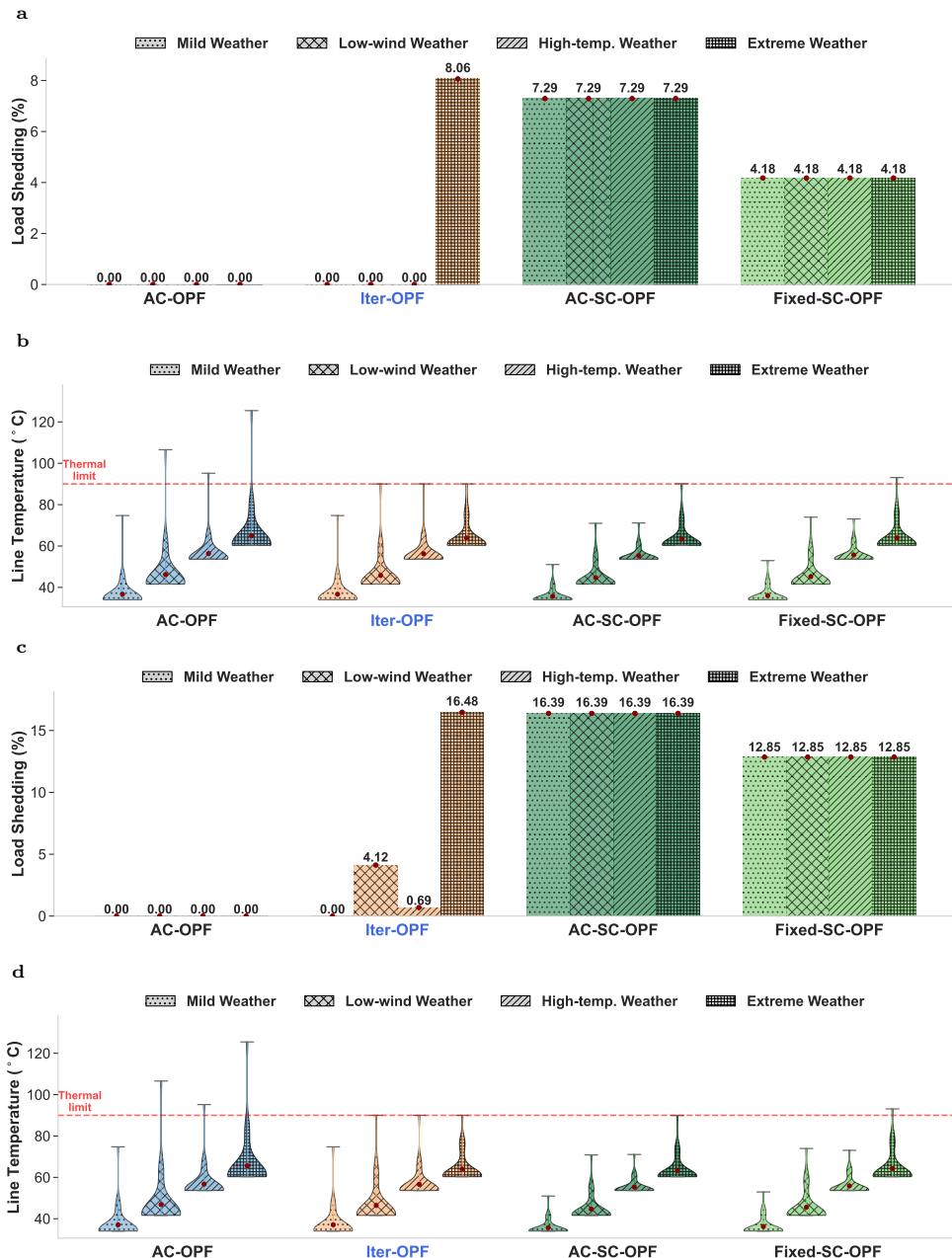
493 At 0.9 load ratio, AC-OPF achieves zero load shedding across all scenarios but pro-
494 duces thermal violations under high-temperature and extreme conditions (Fig. 29b).
495 Iter-OPF maintains zero load shedding under mild, low-wind, and high-temperature
496 conditions, increasing to 8.06% only under extreme weather—reflecting the com-
497 pounded effect of reduced convective cooling and elevated ambient temperature.
498 Security-constrained formulations require constant load shedding under all conditions
499 (7.29% for AC-SC-OPF; 4.18% for Fixed-SC-OPF), demonstrating their inability to
500 exploit favorable weather conditions.

501 At 1.0 load ratio, these patterns intensify (Fig. 29c,d). AC-OPF maintains zero load
502 shedding but with thermal violations exceeding 120°C—well beyond safe operating
503 limits. Iter-OPF exhibits weather-responsive behavior: 0% load shedding under mild
504 conditions, 4.12% under low-wind, 0.69% under high-temperature, and 16.48% under
505 extreme conditions. Security-constrained approaches show weather-invariant curtail-
506 ment (16.39% for AC-SC-OPF; 12.85% for Fixed-SC-OPF), over-curtailing under mild
507 conditions while providing no additional protection during stress events.

508 These results demonstrate that compound weather effects—the simultaneous
509 occurrence of high temperature and low wind speed—cannot be adequately addressed
510 by static security margins. Our thermal-aware formulation enables weather-adaptive
511 dispatch that maximizes grid efficiency under favorable conditions while ensuring safe
512 operation during compound stress events. This capability is particularly valuable as
513 climate projections indicate increasing co-occurrence of heat extremes and atmospheric
514 stagnation.



Supplementary Figure 28 | Thermal analysis results for the IEEE 30-bus system under different load and weather conditions. **a** Load shedding percentage across model formulations under mild and extreme weather conditions. **b** Distribution of line temperatures across all transmission lines; the red dashed line indicates the thermal limit (90°C). **c** Computational running time for each formulation. Error bars represent standard deviation across test instances.



Supplementary Figure 29 | Sensitivity analysis results for the IEEE 30-bus system under different load and weather conditions. **a-b** Load shedding percentage and line temperature distribution at 0.9 load ratio. **c-d** Load shedding percentage and line temperature distribution at 1.0 load ratio. The red dashed line indicates the thermal limit (90°C).

515 References

- 516 [1] Hörsch, J., Hofmann, F., Schlachtberger, D. & Brown, T. Pypsa-eur: An open
517 optimisation model of the european transmission system. *Energy strategy reviews*
518 **22**, 207–215 (2018).
- 519 [2] Hersbach, H. *et al.* The era5 global reanalysis. *Quarterly journal of the royal*
520 *meteorological society* **146**, 1999–2049 (2020).
- 521 [3] Copernicus Climate Change Service. Climate and energy indicators
522 for europe from 2005 to 2100 derived from climate projections (2021).
523 URL <https://cds.climate.copernicus.eu/datasets/sis-energy-derived-projections?tab=overview>. Accessed: 2024-10-06.
- 525 [4] Hirth, L., Mühlenpfordt, J. & Bulkeley, M. The entso-e transparency platform—a
526 review of europe’s most ambitious electricity data platform. *Applied energy* **225**,
527 1054–1067 (2018).
- 528 [5] Staffell, I., Pfenninger, S. & Johnson, N. A global model of hourly space heating
529 and cooling demand at multiple spatial scales. *Nature Energy* 1–17 (2023).
- 530 [6] Hofmann, F., Hampp, J., Neumann, F., Brown, T. & Hörsch, J. Atlite: a
531 lightweight python package for calculating renewable power potentials and time
532 series. *Journal of Open Source Software* **6**, 3294 (2021).
- 533 [7] Cain, M. B., O’neill, R. P., Castillo, A. *et al.* History of optimal power flow and
534 formulations. *Federal Energy Regulatory Commission* **1**, 1–36 (2012).
- 535 [8] Tang, Y., Dvijotham, K. & Low, S. Real-time optimal power flow. *IEEE*
536 *Transactions on Smart Grid* **8**, 2963–2973 (2017).
- 537 [9] Jabr, R. A., Karaki, S. & Korbane, J. A. Robust multi-period opf with storage
538 and renewables. *IEEE Transactions on Power Systems* **30**, 2790–2799 (2014).
- 539 [10] Capitanescu, F. *et al.* State-of-the-art, challenges, and future trends in security
540 constrained optimal power flow. *Electric power systems research* **81**, 1731–1741
541 (2011).
- 542 [11] Brown, T., Hörsch, J. & Schlachtberger, D. Pypsa: Python for power system
543 analysis. *arXiv preprint arXiv:1707.09913* (2017).
- 544 [12] Hörsch, J., Ronellenfitsch, H., Witthaut, D. & Brown, T. Linear optimal power
545 flow using cycle flows. *Electric Power Systems Research* **158**, 126–135 (2018).
- 546 [13] Frank, S., Sexauer, J. & Mohagheghi, S. Temperature-dependent power flow.
547 *IEEE Transactions on Power Systems* **28**, 4007–4018 (2013).

- 548 [14] Ahmed, A., McFadden, F. J. S. & Rayudu, R. Weather-dependent power flow
 549 algorithm for accurate power system analysis under variable weather conditions.
 550 *IEEE Transactions on power systems* **34**, 2719–2729 (2019).
- 551 [15] Neumann, F., Hagemeyer, V. & Brown, T. Assessments of linear power flow and
 552 transmission loss approximations in coordinated capacity expansion problems.
 553 *Applied Energy* **314**, 118859 (2022).
- 554 [16] Glaum, P. & Hofmann, F. Leveraging the existing german transmission grid with
 555 dynamic line rating. *Applied Energy* **343**, 121199 (2023).
- 556 [17] Abboud, A. W., Gentle, J. P., Parikh, K. & Coffey, J. Sensitivity effects of
 557 high temperature overhead conductors to line rating variables. Tech. Rep., Idaho
 558 National Lab.(INL), Idaho Falls, ID (United States) (2020).
- 559 [18] Karimi, S., Musilek, P. & Knight, A. M. Dynamic thermal rating of transmission
 560 lines: A review. *Renewable and Sustainable Energy Reviews* **91**, 600–612 (2018).
- 561 [19] Manninen, H., Lippus, M. & Rute, G. Dynamic line rating using hyper-
 562 local weather predictions: A machine learning approach. *arXiv preprint*
 563 *arXiv:2405.12319* (2024).
- 564 [20] Ngoko, B. O., Sugihara, H. & Funaki, T. Optimal power flow considering line-
 565 conductor temperature limits under high penetration of intermittent renewable
 566 energy sources. *International Journal of Electrical Power & Energy Systems* **101**,
 567 255–267 (2018).
- 568 [21] Hörsch, J. & Brown, T. *The role of spatial scale in joint optimisations of gen-*
 569 *eration and transmission for european highly renewable scenarios*, 1–7 (IEEE,
 570 2017).
- 571 [22] Neumann, F. & Brown, T. *Heuristics for transmission expansion planning in*
 572 *low-carbon energy system models*, 1–8 (IEEE, 2019).
- 573 [23] Nigol, O. & Barrett, J. Characteristics of acsr conductors at high tempera-
 574 tures and stresses. *IEEE Transactions on Power Apparatus and Systems* 485–493
 575 (1981).
- 576 [24] Douglass, D. & Reding, J. Ieee standard for calculating the current-temperature
 577 of bare overhead conductors. *IEEE Standard* 738–2006 (2007).
- 578 [25] ENTSO-E. Technologies for transmission system. Technical Report, Euro-
 579 pean Network of Transmission System Operators for Electricity (2018).
 580 URL <https://eepublicdownloads.blob.core.windows.net/public-cdn-container/clean-documents/tyndp-documents/TYNDP2018/consultation/Technical/Technologies4TS.pdf>. TYNDP 2018.

- 583 [26] Brown, T., Schierhorn, P.-P., Tröster, E. & Ackermann, T. Optimising the euro-
 584 pean transmission system for 77% renewable electricity by 2030. *IET Renewable*
 585 *Power Generation* **10**, 3–9 (2016).
- 586 [27] Duan, Q. *et al.* Pypop7: A pure-python library for population-based black-box
 587 optimization. *Journal of Machine Learning Research* **25**, 1–28 (2024).
- 588 [28] Ieee standard for calculating the current-temperature relationship of bare over-
 589 head conductors. *IEEE Std 738-2012 (Revision of IEEE Std 738-2006 -*
 590 *Incorporates IEEE Std 738-2012 Cor 1-2013)* 1–72 (2013).
- 591 [29] Kanálik, M., Margitová, A., Urbanský, J. & Beňa, L. *Temperature calculation of*
 592 *overhead power line conductors according to the cigre technical brochure 207*, 1–5
 593 (IEEE, 2019).
- 594 [30] ENTSO-E. High temperature low sag conductors (htls). Techno-
 595 pedia. URL [https://www.entsoe.eu/Technopedia/techsheets/
 596 high-temperature-low-sag-conductors-htls](https://www.entsoe.eu/Technopedia/techsheets/high-temperature-low-sag-conductors-htls). Technical Sheet.
- 597 [31] Yang, W. *et al.* Thermal analysis for multi-conductor bundle in high voltage over-
 598 head transmission lines under the effect of strong wind. *Electric Power Systems*
 599 *Research* **231**, 110308 (2024).
- 600 [32] Ngoko, B., Sugihara, H. & Funaki, T. *A temperature dependent power flow model*
 601 *considering overhead transmission line conductor thermal inertia characteristics*,
 602 1–6 (IEEE, 2019).
- 603 [33] Muratori, B. Ieee standard for calculating the current-temperature relationship
 604 of bare overhead conductors. *IEEE Standard 738-2012* (2013).
- 605 [34] Capitanescu, F., Glavic, M., Ernst, D. & Wehenkel, L. Contingency filtering tech-
 606 niques for preventive security-constrained optimal power flow. *IEEE Transactions*
 607 *on Power Systems* **22**, 1690–1697 (2007).
- 608 [35] Ahmed, A., Massier, T., McFadden, F. S. & Rayudu, R. *Weather-dependent ac*
 609 *power flow algorithms*, 1–8 (IEEE, 2020).